Essential role of hyperacetylated microtubules in innate immunity escape orchestrated by the EBV-encoded BHRF1 protein

Damien Glon[1], Géraldine Vilmen[1,2†], Daniel Perdiz[3†], Eva Hernandez[1], Guillaume Beauclair[1], Frédérique Quignon[4], Clarisse Berlioz-Torrent[5], Vincent Maréchal[2], Christian Poüs[3,6], Marion Lussignol[1#] and Audrey Esclatine[1#*]

1. Université Paris-Saclay, CEA, CNRS, Institute for Integrative Biology of the Cell (I2BC), 91198, Gif-sur-Yvette, France.
2. CRSA, Centre de Recherche Saint-Antoine, UMR-S 938, INSERM, Sorbonne Université, 75012 Paris, France
3. INSERM UMR-S 1193, Université Paris-Saclay, 92296 Châtenay-Malabry, France
4. Sorbonne Université, CNRS UMR 144, Institut Curie Centre de Recherche, Paris, France
5. Université de Paris, Institut Cochin, INSERM, CNRS, F-75014 Paris, France
6. Biochimie-Hormonologie, APHP, Hôpitaux Universitaires Paris-Saclay, Site Antoine Béclère, 92141 Clamart, France

[†] These authors contributed equally to this work.

[#] These authors share senior authorship.

* For correspondence: audrey.esclatine@universite-paris-saclay.fr (AE)

Competing interests: The authors declare that no competing interests exist.

Abstract

Innate immunity constitutes the first line of defense against viruses, in which mitochondria play an important role in the induction of the interferon (IFN) response. BHRF1, a multifunctional viral protein expressed during Epstein-Barr virus reactivation, modulates mitochondrial dynamics and disrupts the IFN signaling pathway. Mitochondria are mobile organelles that move through the cytoplasm thanks to the cytoskeleton and in particular the microtubule (MT) network. MTs undergo various post-translational modifications, among them tubulin acetylation. In this study, we demonstrated that BHRF1 induces MT hyperacetylation to escape innate immunity. Indeed, the expression of BHRF1 induces the clustering of shortened mitochondria next to the nucleus. This “mito-aggresome” is organized around the centrosome and its formation is MT-dependent. We also observed that the α-tubulin acetyltransferase ATAT1 interacts with BHRF1. Using ATAT1 knockdown or a non-acetylatable α-tubulin mutant, we demonstrated that this hyperacetylation is necessary for the mito-aggresome formation. Similar results were observed during EBV reactivation. We investigated the mechanism leading to the clustering of mitochondria, and we identified dyneins as motors that are required for mitochondrial clustering. Finally, we demonstrated that BHRF1 needs MT hyperacetylation to block the induction of the IFN response. Moreover, the loss of MT hyperacetylation blocks the localization of autophagosomes close to the mito-aggresome, impeding BHRF1 to initiate mitophagy, which is essential to inhibiting the signaling pathway. Therefore, our results reveal the role of the MT network, and its acetylation level, in the induction of a pro-viral mitophagy.

38 ## Introduction

39 The innate immune system provides the first line of defense against different invading pathogens. This
40 process is based on the sensing of motifs from the foreign organism, called the pathogen-associated
41 molecular pattern (PAMP), by different host pattern recognition receptors (PRR). In the case of a viral
42 infection, their recognition notably leads to the induction of the interferon (IFN) response, which
43 induces the expression of interferon-stimulated genes and the synthesis of cytokines known for their
44 antiviral properties (Lee and Ashkar, 2018).

45 Mitochondria carry out a crucial role in many cellular processes ranging from energy production to
46 programmed cell death, from calcium homeostasis to cell immunity. They constitute a platform for
47 signaling pathways involved in innate immunity thanks to the mitochondrial-resident protein MAVS
48 (mitochondrial antiviral signaling protein), predominantly localized at the mitochondrial outer
49 membrane surface (Arnoult *et al.*, 2011; West *et al.*, 2011). RIG-I (retinoic acid-inducible gene) and
50 MDA5 (melanoma differentiation-associated protein 5), two cytoplasmic PRRs that detect viral
51 genomes, are notably translocated to the mitochondria to interact with MAVS that recruits and
52 activates TBK1 (TANK-binding kinase 1). This kinase is required for the phosphorylation of the
53 transcription factors IRF3 and IRF7 (interferon regulatory factors 3 and 7), leading to the subsequent
54 activation of type I IFN promoter (Arnoult *et al.*, 2011; West *et al.*, 2011). The functions of mitochondria
55 depend on their morphology, which is in turn dependent upon mitochondrial dynamics, including
56 fission, fusion, and motility. Moreover, mitochondria are actively recruited to specific cellular locations
57 to respond to their functions. In eukaryotic cells, the cytoskeleton and notably microtubules (MTs) play
58 a critical role in the distribution of mitochondria throughout the cytoplasm by facilitating their
59 transport to areas with high metabolic demands (Frederick and Shaw, 2007; Kruppa and Buss, 2021).

60 The MT cytoskeleton is a highly dynamic polymer of α and β-tubulin heterodimers, which is involved
61 in a variety of cellular functions, such as supporting cell structures, maintaining cell polarity, but also
62 allowing the transport of organelles. Moreover, it has been shown that the MT network of virally
63 infected cells could be used for intracellular transport of viral particle/genomic material to the sites of
64 replication or assembly (Zheng *et al.*, 2017). A broad range of MT-associated proteins (MAPs)
65 contributes to regulating MT dynamic behavior. MAPs include kinesins and dyneins, which both allow
66 the positioning of organelles and the long-distance transport of vesicles along MT tracks. Kinesins
67 generally transport their cargos toward the plus-end of MTs at the cell periphery. Conversely, dyneins
68 transport their cargos to the minus-end of MTs in the cell center (Hancock, 2014). The relationship
69 between MTs and mitochondrial transport is not completely understood. Mitochondrial movement
70 involves mitochondrial adaptors such as small mitochondrial Rho GTPases Miro1/2 and TRAK1/2

71 (López-Doménech *et al.*, 2018). Indeed, Miro proteins can engage both kinesin and dynein to mediate
72 the bidirectional movement of mitochondria along MT tracts (Fransson *et al.*, 2006; Frederick and
73 Shaw, 2007; Tang, 2018).

74 MT functions are regulated by numerous post-translational modifications such as acetylation,
75 detyrosination, phosphorylation, methylation or polyglutamylation (Janke and Magiera, 2020). Among
76 them, the acetylation of α-tubulin, which mainly occurs on the Lysine in position 40 (K40), has emerged
77 as an important regulator of numerous cell functions (Perdiz *et al.*, 2011). For example, α-tubulin
78 acetylation, which is often linked to microtubule stabilization, modulates the binding of MAPs
79 (Dompierre *et al.*, 2007; Mackeh *et al.*, 2014; Reed *et al.*, 2006) and therefore may modulate organelle
80 movement. Indeed, stable MTs are particularly involved in mitochondrial transport (Friedman *et al.*,
81 2010), and it has been reported that acetylation of α-tubulin mediates dynein-dependent transport of
82 mitochondria along MTs (Misawa *et al.*, 2013).

83 Our group recently unravelled the novel functions in innate immunity of the Epstein-Barr virus (EBV)
84 BHRF1 protein, a viral Bcl-2 homolog (Khanim *et al.*, 1997), related to its mitochondrial localization
85 (Vilmen *et al.*, 2020). We demonstrated that BHRF1 disturbs mitochondrial dynamics and subsequently
86 stimulates mitophagy, a cellular process that can specifically sequester and degrade mitochondria by
87 autophagy, leading to the inhibition of type I IFN response by EBV (Vilmen *et al.*, 2020). Here, we
88 explored the role of the MT network in the innate immunity escape induced by BHRF1 and we revealed
89 the contribution of the MT hyperacetylation on the BHRF1-induced mitochondrial clustering and on
90 the BHRF1-mediated counteraction of the IFN responses.

Results

BHRF1-induced mito-aggresome is organized around the centrosome

The EBV-encoded BHRF1 localizes to mitochondria, and its expression in HeLa cells dramatically alters mitochondrial dynamics and distribution, (Vilmen *et al.*, 2020). By confocal microscopy, we observed abnormal mitochondrial clusters close to the nucleus in BHRF1-expressing cells, whereas in control cells (empty vector [EV] transfection), mitochondria remained distributed throughout the cytoplasm (***Figure 1A***). This mitochondrial phenotype, known as "mito-aggresome", was in accordance with our previous observations. To quantify this phenotype, we arbitrarily considered that, when the compaction index (CI) of mitochondria is above 0.4, the cell presents a mito-aggresome, whereas when the CI value is below 0.4, mitochondria are distributed homogeneously throughout the cell cytoplasm (Narendra *et al.*, 2010; Vilmen *et al.*, 2020). The expression of BHRF1 significantly increased the CI values, which corresponds to the formation of a mito-aggresome in almost 80% of the cells (***Figure 1B***). To confirm the role of BHRF1 in the context of EBV infection, we analyzed the mitochondrial phenotype in EBV-positive Akata B cells, during latency or after treatment with anti-human IgG to induce EBV reactivation (***Figure 1 – figure supplement 1***). We clearly observed mito-aggresomes upon EBV reactivation, whereas the knockdown (KD) of BHRF1 completely blocked their formation. Since BHRF1 is associated with mitochondrial fragmentation (***Figure 1A - insets***), we precisely evaluated mitochondrial shape by calculation of the aspect ratio (AR) and the form factor (FF), two parameters that reflect the mitochondrial length and the branching of mitochondria, respectively. As calculated in ***Figure 1C***, BHRF1 expression significantly reduced both AR and FF parameters, confirming the induction of mitochondrial fission.

As mitochondria localize near the nucleus upon BHRF1 expression, the involvement of the MT network in this mitochondrial redistribution was investigated. In mammalian cells, mitochondria move along cytoskeletal tracks to sites of high-energy demand in an MT-dependent manner (Detmer and Chan, 2007). At interphase, the MT network radiates from the centrosome, the main MT organizing center for directing the polarity and the orientation of MTs. By co-staining BHRF1-expressing cells for mitochondria and pericentrin, a classical centrosomal marker, we observed that mitochondria are concentrated around the centrosome to form a mito-aggresome (***Figure 1D***). Moreover, a 3D reconstruction confirmed the clustering of BHRF1 in the vicinity of the nucleus around the centrosome (***Figure 1 – figure supplement 2***).

The MT network is required for BHRF1-induced mito-aggresome formation

To test whether MTs play a role in the mitochondrial redistribution induced by BHRF1 expression, the whole MT network was disassembled using a treatment mixing nocodazole, a classical MT-destabilizing

124 drug, and exposure to cold (Geeraert *et al.*, 2010). As shown in ***Figure 1E - left panel*** this treatment
125 disassembled MTs (fuzzy staining of α-tubulin). The removal of nocodazole followed by 1 hour in a
126 warm complete medium at 37°C restored the MT network (***Figure 1E - right panel***). In cells without
127 BHRF1 expression, mitochondria were homogeneously distributed in the cytoplasm, and the
128 disorganization of the MT network had no impact on their distribution. Conversely, when MTs were
129 depolymerized, the mito-aggresome formation was abolished (***Figure 1E - left panel***) and mitochondria
130 were then distributed throughout the cell (CI values mainly below 0.4). This phenomenon was
131 reversible since the mitochondria rapidly re-aggregated to different extents within 1 hour after
132 reassembly of the MT network (most of the CI values above 0.4) (***Figure 1E - right panel***). In contrast,
133 mitochondria in non-transfected neighboring cells remained scattered within the cytoplasm after
134 nocodazole removal. The quantification of mito-aggresomes in BHRF1-positive cells showed that
135 whereas less than 20% of the cells presented mitochondrial clustering after depolymerization
136 treatment (***Figure 1F***), this proportion went back to more than 50% after repolymerization of the MTs
137 (compare to 80% without treatment). We concluded that the MT network is required for the mito-
138 aggresome formation.

139 The actin network is also known to be involved in mitochondrial transport and fission (De Vos *et al.*,
140 2005; López-Doménech *et al.*, 2018). We thus checked if F-actin disorganization affects the
141 mitochondrial phenotype induced by BHRF1. To do so, we treated HeLa cells with cytochalasin B to
142 disrupt F-actin but we did not observe any changes in the mitochondrial phenotype in BHRF1-positive
143 cells (***Figure 1 – figure supplement 3A***). BHRF1 still induced mito-aggresome formation and fission at
144 the same level as in the control (***Figure 1 – figure supplement 3B***). Therefore, the actin network does
145 not seem to be involved in the mitochondrial phenotype.

146 **EBV reactivation induces BHRF1-dependent MT hyperacetylation**

147 We next explored whether BHRF1 could modify the MT network by assessing α-tubulin acetylation
148 level. Interestingly, upon BHRF1 expression, whereas α-tubulin staining was unchanged, acetyl-α-
149 tubulin was redistributed and colocalized with BHRF1 (***Figure 2A***). Moreover, we observed a brighter
150 signal of acetyl-α-tubulin in BHRF1 expressing cells, suggesting an increase in α-tubulin acetylation.
151 This was confirmed by western-blot analysis showing an increase of 60% under BHRF1 expression
152 (***Figure 2B***).

153 To confirm these results in the context of EBV infection, we analyzed the level of MT acetylation in
154 EBV-positive Akata B cells (***Figures 2C and 2E***). We used, as a control, EBV-negative Ramos B cells
155 similarly treated with anti-IgG. We observed an increase of MT acetylation only 24h after EBV
156 reactivation in Akata cells (visualized by Ea-D and ZEBRA viral protein expression). This MT

157 hyperacetylation coincided with BHRF1 expression. We confirmed that BHRF1 is required for this
158 phenotype in the context of EBV infection of B cells, using an shRNA targeting BHRF1 (***Figures 2D and***
159 ***2E***). In parallel, in HEK293/EBV+ epithelial cells, the EBV genomes WT and ΔBHRF1 were reactivated by
160 co-transfection of plasmids encoding the trans-activator proteins ZEBRA and Rta (***Figures 2F and 2G***).
161 We similarly observed a BHRF1-dependent MT hyperacetylation upon EBV reactivation in epithelial
162 cells. Due to a low EBV reactivation rate in this model, the increase of MT hyperacetylation observed,
163 although statistically significant, was less important than in Akata cells. However, by confocal
164 microscopy, the increase of tubulin acetylation was clearly seen in WT HEK293/EBV+ and not in
165 ΔBHRF1 (***Figure 2G***).

166 **MT hyperacetylation is required for the mito-aggresome formation**

167 To determine whether this hyperacetylation could be involved in BHRF1-induced mitochondrial
168 alterations, we expressed in HeLa cells a non-acetylatable α-tubulin mutant (mCherry-α-tubulin K40A)
169 which prevents MT hyperacetylation (Dompierre *et al.*, 2007). Expression of this non-acetylatable α-
170 tubulin mutant does not alter the MT network architecture and this protein is incorporated in the
171 whole MT network (Geeraert *et al.*, 2010). However, the whole MT network hyperacetylation is
172 prevented, since α-tubulin acetylation only occurs on polymers and the MT network is totally
173 decorated with this non-acetylatable α-tubulin. We thus verified by immunoblot analysis that BHRF1
174 was unable to induce hyperacetylation of α-tubulin when the α-tubulin K40A mutant was expressed
175 (***Figure 3 – figure supplement 1A***). Then, the impact of α-tubulin K40A on the clustering of
176 mitochondria was analyzed by confocal microscopy (***Figures 3A and 3B***). In cells co-expressing α-
177 tubulin K40A and BHRF1, CI mean value was below 0.4 and mitochondria were homogeneously
178 distributed throughout the cytoplasm, similarly to control cells. Thus, we concluded that BHRF1-
179 induced mito-aggresome formation depends on MT hyperacetylation. This was confirmed in the
180 context of EBV reactivation (***Figures 3C and 3D***). EBV reactivation was visualized in HEK293/EBV WT
181 cells using the staining of Ea-D viral protein.

182 Interestingly, we observed that without α-tubulin hyperacetylation, BHRF1 expression or EBV
183 reactivation were still able to promote mitochondrial fragmentation (***Figures 3B and 3D***). Confocal
184 images (***Figure 3A, insets***) clearly showed that mitochondria were drastically smaller upon BHRF1
185 expression in both WT and K40A conditions. We previously reported that knockdown of Drp1
186 (dynamin-related protein 1), a master regulator of mitochondrial fission, prevents the BHRF1-induced
187 mitochondrial phenotype (Vilmen *et al.*, 2020). We thus investigated the role of Drp1 in MT
188 hyperacetylation and found that the loss of Drp1 inhibits MT hyperacetylation induced by BHRF1
189 expression (***Figure 3 – figure supplement 2A***). In the same way, treatment of Akata cells with Mdivi-1,
190 which inhibits mitochondrial fission, blocked MT hyperacetylation induced by EBV reactivation (***Figure***

191 ***3 – figure supplement 2B***). Taken together, these results demonstrated that the hyperacetylation of
192 MTs requires mitochondrial fission and is essential for BHRF1-induced mito-aggresome formation.

193 **MT hyperacetylation is necessary for the inhibition of type I IFN response by BHRF1**

194 Mitochondria appear to be central organelles for the induction of antiviral innate immunity. Our group
195 and others previously demonstrated that impairing the mitochondrial morphodynamics leads to the
196 inhibition of IFN response (Castanier *et al.*, 2010; Chatel-Chaix *et al.*, 2016; Vilmen *et al.*, 2020;
197 Yoshizumi *et al.*, 2014). Considering the importance of tubulin hyperacetylation for the formation of
198 mito-aggresomes, we investigated whether MT hyperacetylation was required for the inhibition of
199 type I IFN response by BHRF1. We first performed an IFN-β promoter-driven luciferase reporter assay
200 in BHRF1-expressing HEK293T cells (***Figure 4A***). The activation of the IFN-signaling pathway was
201 induced by transfection of an active form of RIG-I, designated ΔRIG-I (2xCARD) (Yoneyama *et al.*, 2004),
202 which constitutively activates the MAVS-dependent pathway through CARD domains interaction. As
203 previously observed, BHRF1 dramatically blocked the IFN-β promoter activation. By contrast, the
204 expression of the α-tubulin K40A significantly prevented this inhibition (***Figure 4A***). To confirm our
205 results, we next examined the cellular localization of IRF3 by immunofluorescence. In basal conditions,
206 IRF3 staining is diffuse throughout the cytoplasm. When ΔRIG-I (2xCARD) is expressed, IRF3
207 translocates from the cytoplasm into the nucleus but the expression of BHRF1 blocked this
208 translocation (***Figure 4B***). However, when MT hyperacetylation was prevented, BHRF1 was not able to
209 block IRF3 nuclear translocation (***Figure 4B***). Quantification of this assay showed that expression of the
210 non-acetylatable form of α-tubulin totally restored IRF3 nuclear translocation upon BHRF1 expression
211 (***Figure 4C***). Therefore, our results demonstrated that MT hyperacetylation is required for BHRF1 to
212 inhibit type I IFN response.

213 We investigated whether this strategy of IFN inhibition through MT hyperacetylation was original and
214 specific to BHRF1. To explore this, we assayed the impact of three different mitophagy inducers,
215 AMBRA1-ActA, Oligomycin/Antimycin A (O/A) and carbonyl cyanide m-chlorophenyl hydrazone
216 (CCCP), on the interplay between tubulin acetylation and IFN inhibition (Lazarou *et al.*, 2015; Narendra
217 *et al.*, 2008; Strappazzon *et al.*, 2015) (***Figure 4 – figure supplement 1***). Similar to BHRF1, expression
218 of AMBRA1-ActA induced mitochondrial fission and mito-aggresome formation, leading to IFN
219 inhibition (***Figure 4 – figure supplement 1A and 1E***). However, AMBRA1-ActA did not impact tubulin
220 acetylation (***Figure 4 – figure supplement 1B***). On the contrary, the mitophagy inducers O/A and CCCP
221 did not induce mito-aggresome formation, although CCCP increased mitochondrial fission (***Figure 4 –***
222 ***figure supplement 1C***). These two treatments were able to reduce IFN production, through mitophagy
223 induction. Indeed, treatment with chloroquine (CQ), which blocks autophagic degradation, restored
224 the IFN level (***Figure 4 – figure supplement 1E***). Similar to AMBRA1-ActA, neither O/A nor CCCP

225 impacted tubulin acetylation (***Figure 4 – figure supplement 1D***). These data, summarized in ***Figure 4 –***
226 ***figure supplement 1F***, clearly showed that these three mitophagy inducers blocks IFN response, but
227 without regulating MT acetylation level. This demonstrates the originality of BHRF1 strategy to inhibit
228 IFN but also the fact that more generally the induction of mitophagy can impede IFN production.

229 **BHRF1 requires acetyltransferase ATAT1 to modify MTs and form mito-aggresomes.**

230 Thereafter, we wanted to characterize the mechanism of MT hyperacetylation induction by BHRF1.
231 Tubulin acetylation results from the balance between the activities of tubulin acetyltransferases and
232 deacetylases. Therefore, a hyperacetylation of the MTs can be the consequence of either the inhibition
233 of deacetylases or the activation of an acetyltransferase. First of all, we explored a potential inhibitory
234 role of BHRF1 on the two main α-tubulin deacetylases, HDAC6 (histone deacetylase 6) and SIRT2
235 (sirtuin type 2) (Hubbert *et al.*, 2002; North *et al.*, 2003). Indeed, it has been observed that KD of SIRT2
236 results in an aberrant mitochondrial distribution in the perinuclear region (Misawa *et al.*, 2013), and
237 another study showed that the depletion of SIRT2 results in nuclear envelope shape defects (Kaufmann
238 *et al.*, 2016). These observations are clearly similar to the effect of BHRF1 on mitochondria, as well as
239 its distribution around the nuclear envelope and the modification of the nucleus shape (***Figure 1A***).
240 We thus performed an *in vitro* tubulin deacetylation assay (Mackeh *et al.*, 2014). This test consists of
241 mixing the highly acetylated porcine brain tubulin with lysates of BHRF1-expressing cells. Lysate of
242 control EV-transfected cells reduced the acetylation of tubulin by approximately 50% compared to the
243 condition without cell lysate (***Figure 5A***). The same deacetylase activity was observed with BHRF1-
244 positive lysates, indicating that BHRF1 does not inhibit the deacetylases.

245 We subsequently investigated the role of ATAT1 (alpha-tubulin N-acetyltransferase 1) on BHRF1-
246 induced MT hyperacetylation (Shida *et al.*, 2010). We knocked down ATAT1 expression by a siRNA
247 approach and observed no more detectable acetylation activity under BHRF1 expression (***Figure 5B***),
248 suggesting the involvement of ATAT1 in BHRF1-induced hyperacetylation. Then, we checked the
249 mitochondrial network and observed that ATAT1 KD prevents mito-aggresome formation but not
250 mitochondrial fission (***Figures 5C and 5D***). These results led us to conclude that BHRF1 activates the
251 acetyltransferase ATAT1, leading to MT hyperacetylation and subsequent mito-aggresome formation.
252 To go further, we analyzed the distribution of GFP-tagged ATAT1 in presence of BHRF1 in HeLa cells
253 (***Figure 5 – figure supplement 2***) and we observed a clear colocalization between GFP-ATAT1 and
254 BHRF1 and, in all cells expressing GFP-ATAT1, a predictable increase in tubulin acetylation. Finally, co-
255 immunoprecipitation assays revealed that BHRF1 interacts with ATAT1 in HeLa cells (***Figures 5E and***
256 ***5F***). Our results suggest that the interaction between BHRF1 and ATAT1 leads to MT hyperacetylation.

257 **Mito-aggresome formation requires retrograde transport of mitochondria via dyneins**

258 We observed in ***Figure 1E*** that after removal of nocodazole and regrowth of the MT network,
259 mitochondria rapidly re-aggregated in BHRF1-expressing cells, suggesting that an MT-dependent
260 motor activity is involved in the mito-aggresome formation. The hyperacetylation of MTs has been
261 previously shown to facilitate the recruitment and binding of MAPs on the tubulin (Dompierre *et al.*,
262 2007). We therefore hypothesized that BHRF1-induced mitochondrial clustering next to the nucleus
263 could use dyneins. To investigate this hypothesis, we inhibited dynein functions by overexpression of
264 p50-dynamitin. The overexpression of one subunit of the dynactin complex (p50-dynamitin) disrupts
265 it and results in the dissociation of dyneins from the MT network. We observed that the expression of
266 this construction totally prevents mito-aggresome formation in BHRF1-expressing cells (***Figures 6A and***
267 ***6B***). Moreover, the ability of BHRF1 to induce mitochondrial fission was decreased when dyneins were
268 inhibited, as we observed a partial but significant restoration of mitochondrial fission parameters (AR
269 and FF; ***Figure 6B***).

270 To confirm the importance of dynein motors in the mito-aggresome formation, we treated cells with
271 ciliobrevin-D, a specific inhibitor of dyneins, which blocks their gliding along MTs and their ATPase
272 activity. As with overexpression of p50-dynamitin, BHRF1 was not able to induce mito-aggresomes in
273 cells treated with ciliobrevin-D (***Figure 6 – figure supplement 1B and 1C***). However, BHRF1 still induced
274 a slight mitochondrial fission phenomenon. Altogether, these results demonstrated that fragmented
275 mitochondria are clustered next to the nucleus in a dynein-dependent manner.

276 **MT hyperacetylation does not affect BHRF1-pro-autophagic activity, but is required for the**
277 **first step of mitophagy induction**

278 Our group previously demonstrated that BHRF1 first stimulates autophagy and then induces
279 mitophagy, the selective degradation of mitochondria (Vilmen *et al.*, 2020). Autophagy is a conserved
280 cellular process allowing the removal and recycling of damaged or supernumerary cellular
281 components. This process involves double-membrane vesicles, called autophagosomes, which fuse
282 with lysosomes to degrade the content. Selective autophagy consists of the recognition of a specific
283 cargo by a molecular receptor that links the cargo to the autophagosome for its removal (Green and
284 Levine, 2014).

285 Several studies demonstrated the role of MTs during the autophagic process, notably during the
286 formation of the autophagosomes (Geeraert *et al.*, 2010; Köchl *et al.*, 2006; Mackeh *et al.*, 2013). Thus,
287 we investigated whether BHRF1 required MT hyperacetylation to induce autophagy. The autophagic
288 flux was studied in HeLa cells co-expressing α-tubulin K40A and BHRF1. We first analyzed by
289 immunofluorescence the accumulation of LC3 (microtubule-associated protein 1 light chain 3), a

290 classical marker of autophagosomes in the presence or absence of CQ, an inhibitor of the autophagic
291 flux. Expression of BHRF1 induced a clear accumulation of LC3 dots in the cytoplasm, and even more
292 after CQ treatment, when non-acetylatable α-tubulin was expressed (***Figure 7A***). We quantified LC3
293 dots and we observed no difference when MTs were hyperacetylated or not (***Figure 7B and Figure 7 –***
294 ***figure supplement 1B***). We confirmed the result by analyzing the accumulation of lipidated LC3 (LC3-
295 II) by immunoblot and we observed an increase in LC3-II levels in BHRF1-expressing cells,
296 independently of MT hyperacetylation (***Figure 7C and Figure 7 – figure supplement 1C***). This increase
297 is potentiated after CQ treatment. Therefore, we concluded that BHRF1 stimulates the biogenesis of
298 autophagosomes and the autophagic flux independently of MT hyperacetylation.

299 Intriguingly, we noticed that the autophagosomes were localized close to the nucleus upon BHRF1
300 expression (***Figure 7D***). MT hyperacetylation is required for this juxtanuclear localization, suggesting
301 its involvement in BHRF1-induced mitophagy. We therefore investigated the colocalization between
302 mitochondria and autophagosomes in cells co-expressing α-tubulin K40A and BHRF1. When MT
303 hyperacetylation was prevented, mitochondria did not colocalize anymore with autophagosomes
304 (***Figure 7E***). The quantification of colocalization intensity, measured by Manders' coefficient,
305 confirmed that mitochondrial sequestration in autophagic vesicles did not occur when the mito-
306 aggresome formation was impeded (***Figure 7F***). Altogether, this suggests that BHRF1-induced MT
307 hyperacetylation triggers the localization of autophagosomes in the close vicinity of mitochondria.

308 **Autophagy is required for MT hyperacetylation**

309 Our results demonstrated that the level of tubulin acetylation does not impact BHRF1-induced
310 autophagy. We then decided to investigate whether, conversely, autophagy was involved in MT
311 hyperacetylation. We first observed that inhibition of autophagy by treatment with 3-methyladenine
312 (3-MA) or spautin-1 impeded the MT hyperacetylation (***Figure 8A***). To reinforce this finding, we used
313 a genetic approach. We generated an ATG5 knockout (KO) cell line using a CRISPR/Cas9 approach,
314 which is deficient for autophagy (***Figure 8B***). We observed that in ATG5 KO cells, BHRF1 was unable to
315 increase the tubulin acetylation (***Figure 8C***). Moreover, mito-aggresome formation is dramatically
316 decreased in autophagy-deficient cells (***Figures 8D and 8E***), in accordance with our previous results in
317 presence of autophagy inhibitors (Vilmen *et al.*, 2020). To confirm whether autophagy was also
318 required during EBV reactivation, we treated Akata cells with spautin-1. We observed the lack of MT
319 hyperacetylation (***Figure 8 – figure supplement 1A***) and of mito-aggresome formation (***Figure 8 –***
320 ***figure supplement 1B and 1C***) in EBV-reactivated treated cells.

321 Taken together, our results demonstrated that BHRF1 needs autophagy activation to induce MT
322 hyperacetylation. Therefore, we uncovered a novel mechanism to counteract antiviral immunity,
323 involving the initiation of mitophagy through the induction of tubulin hyperacetylation by BHRF1.

Discussion

Numerous strategies are used by viruses to counteract or evade the innate immune response. We describe here a novel mechanism for viral immune escape. We report for the first time that a post-translational modification of the cytoskeleton, MT hyperacetylation induced by EBV-encoded BHRF1, can block IFN production (***Figure 9***). We previously demonstrated that BHRF1 blocks the IFN response by modifying the mitochondrial dynamics and by stimulating autophagy (Vilmen *et al.*, 2020). Expression of this viral protein induces mitochondrial fission, followed by the delocalization of fragmented mitochondria close to the nucleus in the proximity of the centrosome (***Figure 1 and Figure 1 – figure supplement 2***). Mitochondria are usually driven over long distances along MTs by motor proteins, thanks to the Miro/TRAK adaptor complex (Kruppa and Buss, 2021). In this study, we demonstrate that the MT network is hijacked by BHRF1 to ensure the mito-aggresome formation and to consequently block the antiviral innate immunity (***Figures 1 and 4***). We notably observed that disruption of the MT network impedes mitochondrial trafficking to the centrosome, suggesting a dynamic process. In accordance, our results indicate that BHRF1 requires the MT-based motor dynein, that typically moves towards the minus-end of MT, to regroup mitochondria in the juxtanuclear region (***Figure 6 and Figure 6 – figure supplement 1***).

In eukaryotic cells, MTs are generally built from 13 chains of α-β tubulin dimers known as protofilaments. Properties and behaviors of MTs can be modulated by numerous post-translational modifications on both α and β tubulin (Janke and Magiera, 2020; Janke and Montagnac, 2017). We observed that the expression of BHRF1, after either transfection or EBV reactivation, increases the acetylation of α-tubulin on the lysine in position 40 (K40) (***Figure 2***). Moreover, acetylated MTs are required for the mito-aggresome formation and modulates the localization of autophagosomes (***Figures 3 and 7***). Acetylation of α-tubulin subtly changes its structure and disrupts the interaction between adjacent α-tubulins of neighboring protofilaments (Eshun-Wilson *et al.*, 2019). The loss of this connection weakens interactions between protofilaments, which facilitates their sliding and decreases the flexural rigidity of microtubules, making them more resistant to mechanical bending-induced breakage and disassembly (Portran *et al.*, 2017). Moreover, acetylated α-tubulin is more abundant in stable MTs, which are particularly implicated in mitochondrial transport (Friedman *et al.*, 2010). Similar to what was observed with BHRF1, Misawa *et al.* demonstrated that accumulation of acetylated α-tubulin by KD of SIRT2 results in an aberrant mitochondrial distribution in the perinuclear region (Misawa *et al.*, 2013).

Our results demonstrate that BHRF1 induces MT hyperacetylation by activating the acetyltransferase ATAT1. Indeed, BHRF1 interacts with ATAT1 and its KD by siRNA impedes the acetylation of α-tubulin

357 and the mito-aggresome formation (***Figure 5***). Moreover, expression of the non-acetylatable K40A
358 mutant form of tubulin confirmed that tubulin acetylation, and not just ATAT1 activity, is required for
359 the mito-aggresome formation and sequestration of mitochondria in autophagosomes (***Figure 3***). We
360 nevertheless investigated a potential inhibitory role of BHRF1 on tubulin deacetylases. However, our
361 results showed that BHRF1 does not impact the global tubulin deacetylase activity, suggesting that
362 HDAC6 and SIRT2, the two main α-tubulin deacetylases, are not inhibited by BHRF1 (Hubbert *et al.*,
363 2002; North *et al.*, 2003).

364 BHRF1-induced acetylation of α-tubulin could increase dynein recruitment to MTs, facilitating the
365 traffic of fragmented mitochondria and autophagosomes to the centrosome. Indeed, it has been
366 shown that MT hyperacetylation *in vitro* and in cells causes the recruitment of dynein and kinesin-1 to
367 MTs, which notably stimulates anterograde and retrograde transport of organelles in neurons or
368 epithelial cells (Dompierre *et al.*, 2007; Geeraert *et al.*, 2010). We know that BHRF1 interacts with
369 BECN1, a key regulator of autophagosome formation and with BIM, a proapoptotic BH3-only protein
370 expressed at the mitochondrial outer membrane (Desbien *et al.*, 2009; Kvansakul *et al.*, 2010; Vilmen
371 *et al.*, 2020). Moreover, it has been reported that BIM can also interact with the dynein light chain
372 subunit DYNLL1 (Puthalakath *et al.*, 1999; Singh *et al.*, 2019). Interestingly, it has been shown that BIM
373 binds to BECN1, linking BECN1 to dynein via DYNLL1 (Janke and Magiera, 2020; Luo *et al.*, 2012; Roberts
374 *et al.*, 2013). Therefore, we hypothesize that BIM could connect mitochondria to MTs by interacting
375 with BHRF1, BECN1 and DYNLL1. The formation of this putative complex could explain the
376 mitochondrial movement toward the centrosome and participate in autophagy regulation.

377 It is interesting to note that MT hyperacetylation induced by BHRF1 or EBV reactivation is not involved
378 in mitochondrial fission since expression of the non-acetylatable α-tubulin mutant K40A or the KD of
379 ATAT1 have no impact on mitochondrial length or branching parameters (***Figures 3 and 5***). We
380 previously demonstrated that BHRF1 increases mitochondrial fragmentation in a Drp1-dependent
381 manner (Vilmen *et al.*, 2020). Moreover, BHRF1 increases the dephosphorylation of Drp1 in position
382 Ser637, which is then recruited to mitochondria to allow mitochondrial fission (Vilmen *et al.*, 2020). In
383 our context, the lack of direct involvement of acetylated MTs on mitochondrial fission could seem quite
384 surprising, since it has been previously shown that MT hyperacetylation triggered by acute
385 hyperosmotic stress enhanced mitochondrial fission (Perdiz *et al.*, 2017). However, in the context of
386 this acute stress, mitochondrial fission is associated with an increased level of Ser616 phosphorylation
387 of Drp1, a different post-translational modification from the one observed upon BHRF1 expression.
388 The implication of hyperacetylated-MT in the mitochondrial fission process may thus differ according
389 to the type of cellular stress.

390 We observed that BHRF1-induced autophagy is necessary to increase MT acetylation since autophagy
391 deficiency impedes MT acetylation (***Figure 8***). This could seem unexpected since several studies have
392 demonstrated the importance of MT acetylation to induce autophagosome formation and maturation,
393 and the direct correlation between MT acetylation levels and the autophagy flux (Esteves *et al.*, 2019;
394 Geeraert *et al.*, 2010; Xie *et al.*, 2010). For example, starvation-induced autophagy requires MT
395 acetylation to recruit dynein and kinesin-1 on MTs and to allow JNK (c-Jun N-terminal kinase)
396 activation, leading to BECN1 release (Geeraert *et al.*, 2010). Very recently, it has been shown that p27,
397 a tumor suppressor which promotes autophagy in response to glucose starvation, stimulates MT
398 acetylation by binding to and stabilizing ATAT1, to allow the delivery of autophagosomes in the
399 proximity of the centrosome for efficient fusion with lysosomes (Nowosad *et al.*, 2021). However, MTs
400 are not involved in autophagosome formation in basal autophagy (Mackeh *et al.*, 2013). Similarly, we
401 demonstrated that BHRF1-induced MT hyperacetylation has no role in non-selective autophagy.
402 However, we observed that it is essential to induce mitophagy since, in the absence of α-tubulin
403 acetylation, BHRF1 does not induce mitochondrial sequestration into autophagosomes (***Figure 7***). This
404 suggests that the formation of the autophagosomal membranes around mitochondria requires
405 acetylated MTs.

406 Several viral proteins are known to control type I IFN response by stimulating mitophagy (Ding *et al.*,
407 2017; Wang *et al.*, 2019, 2020). The viral glycoprotein (Gn) encoded by Hantaan virus translocates to
408 mitochondria, induces complete mitophagy which leads to MAVS degradation and subsequently
409 impairs innate immune response (Wang *et al.*, 2020). PB1-F2 is a non-structural protein encoded by
410 influenza A virus and constitutively localized to the mitochondrial inner membrane space (Yoshizumi
411 *et al.*, 2014). At mitochondria, the interaction of PB1-F2 with LC3B and mitochondrial TUFM (Tu
412 translation elongation factor) similarly leads to mitophagy induction, MAVS degradation and restrains
413 type I IFN production (Wang *et al.*, 2020). Whether these pro-viral mechanisms depend on the tubulin
414 acetylation level needs to be investigated. Interestingly, we explored the impact of non-viral
415 mitophagy inducers, such as AMBRA1-ActA, CCCP and O/A on MT hyperacetylation and mitochondrial
416 morphodynamics. We demonstrated that they can block IFN production via mitophagy induction,
417 whereas none of them modulated MT acetylation (***Figure 4 – figure supplement 1***). These results
418 clearly demonstrate BHRF1 blocks IFN production by an original mechanism, involving MT acetylation-
419 dependent mitophagy.

420 To conclude, we demonstrated how BHRF1, which is expressed during the early stages of EBV infection
421 and some latency programs associated with lymphomas (Fitzsimmons and Kelly, 2017), reduces innate
422 immunity by manipulating the MT network. We propose a model (***Figure 9***) in which EBV exploits
423 ATAT1-dependent acetylated MTs to modulate mitochondrial morphodynamics, thereby draining

424 fragmented mitochondria toward the centrosome, segregating them from IFN signaling pathways in
425 mitophagosomes to block IFN production. We previously showed that BHRF1 expression induces
426 mitochondrial fission activation and subsequently autophagy stimulation (***Figure 9***). We report here
427 that MT hyperacetylation is downstream of these events. Beyond EBV infection and latency, these
428 findings identify for the first time a role for acetylated MTs in regulating IFN response and innate
429 immunity against viruses.

430 ## Materials and methods

431 ### Antibodies

432 Primary antibodies used in this study included anti-α-tubulin (Sigma-Aldrich, T6199), anti-acetyl-α-
433 tubulin (Sigma-Aldrich, T6793), anti-ATG5 (Sigma-Aldrich, A0731), anti-β-actin (Merck Millipore,
434 MAB1501), anti-BHRF1 (Merck Millipore, MAB8188), anti-c-Myc (Sigma-Aldrich, M4439), anti-Drp1
435 (Cell Signaling Technology, D6C7), anti-Ea-D (Santa Cruz Biotechnology, sc-58121), anti-GFP (Roche,
436 11814460001), anti-GFP (Santa Cruz Biotechnology, sc-9996), anti-HA (Santa Cruz Biotechnology, sc-
437 9082 and sc-7392), anti-IRF3 (Novus Biologicals, SD2062), anti-LC3 (MBL International, PM036 and
438 M151-3B), anti-pericentrin (Sigma-Aldrich, HPA016820), anti-TOM20 (BD Biosciences, 612278), anti-
439 TOM20 (Cell Signaling Technology, D8T4N), anti-ZEBRA (Santa Cruz Biotechnology, sc-53904).
440 Secondary antibodies used in this study included Alexa Fluor 488 goat anti-rabbit, anti-mouse (Jackson
441 ImmunoResearch, 111-545-003, 115-545-003), Alexa Fluor 555 goat anti-rabbit, anti-mouse (Life
442 technology, A21428, A21424), Alexa Fluor 647 donkey anti-rabbit, anti-mouse (Life technology,
443 A31573, A31571). Horseradish peroxidase (HRP)-labeled goat anti-mouse and anti-rabbit secondary
444 antibodies were purchased from Jackson ImmunoResearch Laboratories (115–035–003, 111–035–
445 003).

446 ### Cell culture and transfection

447 HeLa and HEK293T cells were cultured at 37°C under 5% CO_2 in Dulbecco's modified eagle medium
448 (DMEM; Gibco, 41965-039) supplemented with 10% fetal calf serum (FCS; Dominique Dutscher, S181B-
449 500). HeLa cells KD for Drp1 were previously described (Vilmen *et al.*, 2020). ATG5 KO and control cell
450 lines were generated from HeLa cells (see below) and cultured at 37°C under 5% CO_2 in DMEM
451 supplemented with 10% FCS and 1.25 µg/mL of puromycin. Akata cells were grown at 37°C under 5%
452 CO_2 in RPMI-1640 supplemented with 10% FCS and 2 mM of L-Glutamine (Gibco, 25030-081). Cells KD
453 for BHRF1 were generated from Akata cells (see below) and cultured in the same media supplemented
454 with 0.5 µg/mL of puromycin. Ramos cells were kindly provided by Joëlle Wiels (Institut Gustave
455 Roussy, Villejuif, France) and grown in the same way as Akata cells. HEK293/EBV$^+$ cells harboring WT
456 and ΔBHRF1 bacmids were kindly provided by Wolfgang Hammerschmidt (German Research Center
457 for Environmental Health, Munich, Germany) and were cultured at 37°C under 5% CO_2 in DMEM
458 supplemented with 10% FCS and 100 µg/mL of hygromycin B (Invitrogen, 10687010).
459 To reactivate EBV, Akata cells were treated with polyclonal rabbit anti-human IgG (Agilent, A0423) at
460 7.5 µg/mL for 8 or 24 h. To induce EBV productive cycle, HEK293/EBV WT and ΔBHRF1 mutant cells
461 were transfected with ZEBRA and Rta expression plasmid (Altmann and Hammerschmidt, 2005).

462 DNA plasmid transfections were performed using Fugene HD transfection reagent (Promega
463 Corporation, E2311) according to the manufacturer's protocol. One day prior to transfection, cells
464 were seeded in a 24-well plate and incubated at 37°C. On the day of transfection, DNA plasmids were
465 dispersed in opti-MEM (Gibco, 31985-047) and Fugene HD was added to the mix (ratio DNA:Fugene
466 equals 1:3). After incubation for 10 min at room temperature (RT), the transfection mix was added to
467 the cells. Then cells were incubated at 37°C and 6 h post-transfection, DMEM supplemented with 10%
468 FCS was added. Depending on the expression plasmids, cells were fixed 24 h or 48 h post-transfection.

469 **Co-immunoprecipitation assay**

470 HeLa cells were cultured in a 6-well plate and transfected to co-express BHRF1-HA (or EV) and GFP-
471 ATAT1 (or EV). One day after transfection, cells were washed with cold PBS and then lysed at 4°C in
472 RIPA buffer (Thermo Fisher Scientific, 89900) supplemented with a cocktail of protease inhibitors.
473 Then, extracts were centrifuged at 11'000xg at 4°C for 30 min to remove cell debris. Then, BHRF1 or
474 ATAT1 was immunoprecipitated with a rabbit anti-HA antibody (2 µg) or with a mouse anti-GFP
475 antibody (2 µg), respectively. Immunoprecipitations were performed overnight at 4°C. Protein A or G-
476 Sepharose beads (Ademtech, 4230 or 4330) were added for 2 h at 4°C and were washed three times
477 with RIPA buffer. The immune complexes were finally boiled for 10 min in loading buffer (see
478 composition below) before being analyzed by SDS-PAGE.

479 **Dye and drugs**

480 MitoTracker Red CMXRos was purchased from Life Technologies (M7512) and used at 100 nM for 30
481 min before cell fixation to stain the mitochondrial network. Phalloidin was purchased from Sigma-
482 Aldrich (P1951) and used at 20 µg/mL for 1 h to stain F-actin. DAPI was purchased from Thermo Fisher
483 Scientific (D1306) and used at 300 nM to stain dsDNA (nuclei).
484 Nocodazole was purchased from Sigma-Aldrich (M1404) and used at 10 µM to disrupt the MT network.
485 Cytochalasin B was purchased from Sigma-Aldrich (C6762) and used at 10 µg/mL for 30 min to disrupt
486 F-actin. Ciliobrevin D was purchased from Sigma-Aldrich (250401) and used at 40 µM overnight to
487 inhibit cytosolic dyneins. To induce hyperosmotic shock, cells were cultured in media supplemented
488 with 125 mM of NaCl for 30 min. Mdivi-1 was purchased from Sigma Aldrich (M0199) and used at 50
489 µM for 24 h to block Drp1 activity. Autophagic flux was monitored by the addition of CQ (Sigma-Aldrich,
490 C6628) at 50 µM for 2 to 4 h. To inhibit autophagy, we used two different ways: cells were treated
491 either with 3-MA (Sigma-Aldrich, M9281) at 5 mM for 8 h, or with spautin-1 (Sigma-Aldrich, SML0440)
492 at 20 µM for 8 h. To induce mitophagy, cells were treated either during 4 h with CCCP (Sigma-Aldrich,
493 C2759) at 10 µM, or during 6 h with a combination of oligomycin (Millipore, 495455) and antimycin A
494 (Sigma-Aldrich, A8674) at 2.5 µM and 800 nM, respectively.

495 **Extinction of ATAT1 expression**

496 To deplete ATAT1 in HeLa cells, we performed transfection of siRNA directed against ATAT1 encoding
497 mRNA (or non-relevant siRNA as control). We used ON-TARGETplus siRNAs from Dharmacon as a pool
498 of four siRNAs: 5-GUAGCUAGGUCCCGAUAUA-3; 5-GAGUAUAGCUAGAUCCCUU-3; 5-GGGAAACUCACC
499 AGAACGA-3; and 5-CUUGUGAGAUUGUCGAGAU-3. The transfections of siRNA were performed using
500 Oligofectamine reagent (Thermo Fisher Scientific; 12.252.011) according to the manufacturer's
501 protocol and were repeated at days 1, 2, and 3 at a final concentration of 100 nM. At the end of day 3,
502 transfection with BHRF1-HA was also performed using Fugene HD transfection reagent as described
503 above. Cells were then used at day 4 for immunoblotting or immunofluorescence analyses.

504 **Generation of Akata cells KD for BHRF1 expression**

505 To knock down the expression of BHRF1 in Akata cells, we used an shRNA approach delivery through
506 lentivirus transduction. Three different shRNA sequences directed against *BHRF1* mRNA were designed:
507 5'-CCGGGCCAGAGGACACTGTAGTTCTCTCGAGAGAACTACAGTGTCCTCTGGCTTTTTG-3' (Fw, position 123),
508 5'-AATTCAAAAAGCCAGAGGACACTGTAGTTCTCTCGAGAGAACTACAGTGTCCTCTGGC-3' (Rv, position 123),
509 5'-CCGGGTGTTGCTTGAGGAGATAATTCTCGAGAATTATCTCCTCAAGCAACACTTTTTG-3' (Fw, position 154),
510 5'-AATTCAAAAAGTGTTGCTTGAGGAGATAATTCTCGAGAATTATCTCCTCAAGCAACAC-3' (Rv, position 154),
511 5'-CCGGGGCGGCTGGTCTACATTAATTCTCGAGAATTAATGTAGACCAGCCGCCTTTTTG-3' (Fw, position 442),
512 5'-AATTCAAAAAGGCGGCTGGTCTACATTAATTCTCGAGAATTAATGTAGACCAGCCGCC-3' (Rv, position 442).
513 These shRNA sequences were cloned into a pLK0.1-TRC vector, according to Addgene
514 recommendations. To produce recombinant lentiviral particles, HEK293T cells ($3x10^6$ cells) were
515 transfected with 1.5 µg of pLK0.1-TRC/sh-BHRF1 plasmid, 1.125 µg of lentiviral packaging plasmid
516 (psPAX2) and 375 ng of VSV-G envelope expressing plasmid (pMD2.G). Two days after transfection, the
517 cell culture supernatant was collected and filtered (0.45 µm). The lentiviral particle stocks were directly
518 used to transduce target cells by spinoculation method (centrifugation at 800xg at 32°C for 30 min).
519 Three days after transduction, sh-BHRF1 expressing Akata cells were selected by addition of 0.5 µg/mL
520 of puromycin in culture media.

521 **Generation of HeLa cells KO for ATG5 expression**

522 Stock of lentiviral particles were obtained by transfection of HEK293T cells ($2x10^6$ cells) with 2 µg of
523 lentivector plasmid lentiCRISPRv2 (a gift from Feng Zhang, Addgene plasmid, 52961) expressing single
524 guide RNA targeting an exon within ATG5 gene, using Lipofectamine LTX with PLUS Reagent (Life
525 technologies), along with 3 µg of psPAX2 and 1 µg of pMD2.G. The following sequence was used to
526 target ATG5 genes: 5'-AAGATGTGCTTCGAGATGTG-3' (ATG5, exon 1; guide 92). The sequence 5'-
527 GTTCCGCGTTACATAACTTA-3' was used as negative control (referred as CTRL) and previously described

528 (Kearns *et al.*, 2014). Twenty-four hours after transfection, cell media were removed, and cells were
529 cultured for additional 24 h in fresh media. Supernatants were then collected, filtered (0.45 µm) and
530 used to transduce HeLa cells. Three days after transduction, cells were selected by addition of 1.25
531 µg/mL of puromycin in culture media.

532 ***In vitro* tubulin deacetylation assay**

533 Cell lysates of control cells or cells transfected with BHRF1-HA plasmids were prepared using 10 mM
534 Tris buffer pH 8.0, supplemented with 1% Triton, 1 mM NAD^+, and the protease inhibitor cocktail.
535 Lysate aliquots containing 20 µg of proteins were mixed with 2 µg of soluble acetylated tubulin dimers
536 purified from porcine brain (Mackeh *et al.*, 2014; Walker *et al.*, 1988) and adjusted to 50 µL with NAD^+-
537 containing PEM buffer (80 mM PIPES, 2 mM EGTA, 1 mM $MgCl_2$). After 1 h at 37°C, reactions were
538 stopped by adding 4X SDS-PAGE sample buffer and immediately subjected to SDS-PAGE and Western
539 blotting of acetylated and total α-tubulin.

540 **Immunoblot analysis**

541 Cells were lysed in lysis buffer (65 mM Tris, pH 6.8, 4% SDS, 1.5% β-mercaptoethanol, and a cocktail of
542 protease inhibitors) and kept at 100°C for 10 min. Protein extracts were resolved on SDS-PAGE (12.5%)
543 and electro-transferred onto a polyvinylidene difluoride membrane (Amersham, 10600002). After 1h
544 of incubation in blocking buffer (PBS, 0.1% Tween20, and 5% BSA or nonfat dry milk), the membranes
545 were probed overnight at 4°C with primary antibodies. Horseradish peroxidase-labeled antibodies
546 were used as secondary antibody, and revelation was performed using the ECL detection system
547 according to the manufacturer's instructions (Merck Millipore, WBKLS0500). Scanning for
548 quantification of protein levels was monitored using ImageJ software. An anti-β-actin antibody was
549 used to ensure equal loadings and normalize quantification.

550 **Immunofluorescence analysis**

551 For immunofluorescence, adherent cells were cultured on glass coverslips in 24-well plates. The cell
552 monolayers were washed with PBS and cells were fixed with paraformaldehyde (PFA; 4%) in PBS or
553 methanol, depending on the antibodies. The cells were treated with PBS containing NH_4Cl (50 mM) for
554 10 min, permeabilized using PBS, Triton X-100 (0.2%) for 4 min, washed twice with PBS and then
555 incubated for 1 h in PBS, gelatin (0.2%) supplemented with FCS (5%) for blocking. Then the cells were
556 incubated for 1 h with the appropriate primary antibody diluted in PBS, gelatin (0.2%) at RT. Cells were
557 washed three times with PBS and then incubated with the appropriate secondary antibody diluted in
558 PBS, gelatin (0.2%) for 1 h at RT. After washing, the nuclei were counterstained with DAPI. Coverslips
559 were mounted in Glycergel (Agilent Dako, C056330-2) and observed using a Nikon Eclipse 80i
560 epifluorescence microscope (Nikon Instruments) or a Leica TCS SP8 X inverted confocal microscope

561 (Leica, USA). Photographic images were resized, organized, and labeled using Fiji-ImageJ software or
562 LAS AF Lite. Imaris software was also used to perform 3D reconstruction videos.
563 A specific procedure was performed for the colocalization study between mitochondria and
564 autophagosomes. Permeabilization and blocking were performed by incubating the cells for 30 min
565 with PBS, saponin (0.075%; Sigma-Aldrich, 84,510), BSA (1%), and FCS (5%). Antibodies were diluted in
566 PBS, saponin (0.075%), and BSA (1%). In addition, between each antibody incubation, cells were
567 washed twice in PBS, saponin (0.075%), BSA (1%), once with PBS, saponin (0.037%), BSA (0.5%) and
568 twice in PBS. Other steps were the same as described above.
569 To immunostain suspension cells, they were washed once with PBS and diluted at the concentration
570 of 10^6 cells/mL. Then, 15 µL of this cell suspension were dropped on a slide and dried for 10 min at
571 37°C. A circle was drawn around the cell footprint with a hydrophobic PAP pen. Cells were then fixed
572 with PFA (4%), and the next steps were the same as described above.

573 **Luciferase reporter assays to assess IFN-β promoter activity**

574 HEK293T cells were cultured in 24-well plates and transfected for 24 h using Fugene HD, with plasmids
575 encoding the IFN-β luciferase reporter (firefly luciferase; 100 ng), pRL-TK (renilla luciferase; 25 ng),
576 pΔRIG-I (2xCARD) (encoding a positive dominant form of RIG-I; 150 ng), plasmids expressing BHRF1-
577 HA (or EV as control; 150 ng) and mCherry-Tub (WT or K40A; 150 ng). One day after transfection, cells
578 were lysed and measurement of firefly and renilla luciferase activities was performed using the dual-
579 luciferase reporter assay system (Promega Corporation, E1910) according to the manufacturer's
580 protocol. Relative expression levels were calculated by dividing the firefly luciferase values by those of
581 renilla luciferase and normalized to the control condition (without BHRF1-HA expression).

582 **Microtubule depolymerization and repolymerization**

583 To depolymerize MTs, HeLa cells were seeded directly onto glass coverslips and incubated one day
584 before being transfected to express BHRF1. Twenty-four hours after transfection, cells were treated
585 with 10 µM nocodazole (Sigma-Aldrich, M1404) for 2 h at 37°C then 1.5 h at 4°C, to depolymerize the
586 MT network. Cells were immediately PFA 4% fixed and then methanol-permeabilized (t = 0 h before
587 repolymerization). MTs and mitochondria were visualized by immunostaining of α-tubulin and TOM20,
588 respectively. To allow reassembly of the MT network, nocodazole was removed by repeated washes
589 with PBS, and cells were left 1 h in warm complete medium (t = 1 h after MTs regrowth). Cells were
590 then immunostained for BHRF1, TOM20, and α-tubulin.

591 **Mitochondrial phenotype assessment**

592 BHRF1-induced mito-aggresomes were scored by measuring the CI of mitochondrial staining, as we
593 previously described (Vilmen *et al.*, 2020), based on Narendra et al. study (Narendra *et al.*, 2010). We

594 arbitrary determined that a cell presents a mito-aggresome when the CI is above 0.4. The percentage
595 of cells presenting a mito-aggresome was determined by counting at least 20 random cells in each
596 condition from three independent experiments.
597 Mitochondrial morphology was assessed by measuring AR and FF, which are indicators of
598 mitochondrial length and branching, respectively. These parameters were quantified as described
599 before (Koopman *et al.*, 2006). Briefly, on Fiji-ImageJ software, images of mitochondria were convolved
600 using the matrix developed by Koopman, then a threshold was applied to isolate mitochondria from
601 the background. Then cell outline was drawn and mitochondrial phenotype was assessed by the
602 implement analysis particle tool. The AR value is given by the software and corresponds to the ratio
603 between the major and minor axis of the ellipsis equivalent to the mitochondria. The FF value is defined
604 as $(P_{mit}^2)/(4\pi A_{mit})$, where P_{mit} is the length of mitochondrial outline and A_{mit} is the area of mitochondria.
605 The mitochondrial fission parameters were determined by analyzing at least 15 random cells in each
606 condition from three independent experiments.

607 **Plasmids**

608 We previously described the BHRF1-HA expression vector (Vilmen *et al.*, 2020), which was constructed
609 from a pcDNA3.1 expression vector (EV) purchased from Invitrogen (V79020). The mCherry-α-tubulin
610 WT-K40K control vector was kindly provided by Dr. R. Y. Tsien (Howard Hughes Medical Center,
611 University of San Diego, USA) (Shaner *et al.*, 2004) and the mutated vector (mCherry-α-tubulin K40A)
612 was a kind gift from Dr. F. Saudou (Institut Curie, Orsay, France) (Dompierre *et al.*, 2007). The GFP-
613 ATAT1 expression plasmid (27099) and the pLK0.1-TRC cloning vector (10878) were purchased from
614 Addgene. The plasmids Flag-ΔRIG-I (2xCARD) and pIFN-β-Luc were previously described (Yoneyama *et*
615 *al.*, 2004, 1996) and kindly provided by Dr. C. Lagaudrière (I2BC, Gif-sur-Yvette, France). The plasmid
616 pRL-TK was purchased from Promega Corporation (E2241). The p50-dynamitin construct was a gift
617 from Dr. S. Etienne-Manneville (Institut Pasteur, Paris, France) (Etienne-Manneville and Hall, 2001).
618 ZEBRA and Rta expression plasmids were kindly provided by Henri Gruffat (CIRI, Lyon, France). The
619 AMBRA1-ActA expression plasmid was previously described (Strappazzon *et al.*, 2015) and a gift from
620 Flavie Strappazzon. The plasmids psPAX2 (Addgene, 12260) and pMD2.G (Addgene, 12259) come from
621 Didier Trono lab (EPFL, Lausanne, Switzerland).

622 **Results quantification**

623 The number of endogenous LC3 dots per cell was determined using Fiji-ImageJ software. All images
624 were taken with the same microscope settings to allow for comparison. Images were converted into
625 8-bit. Cells' outlines were drawn and nuclei cropped to conserve only the cytoplasm. Thresholding of
626 images was performed to detect only LC3 vesicles. Note that the value of the threshold was conserved

627 and used for each analyzed cell. Finally, the "analyze particles" plug-in was used to count the total
628 number of LC3 dots per cell. For each condition, at least 25 cells were analyzed from three independent
629 experiments.
630 The distance between autophagosomes and the nucleus was measured using Fiji-ImageJ software. For
631 each cell, the distance of all autophagosomes to the nucleus was measured and the mean distance
632 was considered for the statistical analysis. For each condition, at least 20 random cells were analyzed
633 from three independent experiments.
634 The colocalization degree between mitochondrial staining and autophagosomes staining was assessed
635 by measuring Manders split coefficient using the "colocalization threshold" plug-in on Fiji-ImageJ
636 software. For each condition, 30 random cells were analyzed.
637 The proportion of cells presenting an IRF3 nuclear localization was determined by counting at least 50
638 random cells in each condition from three independent experiments.

639 **Statistical analysis**

640 Data are expressed as mean ± standard error of the mean (SEM) and were analyzed with Prism
641 software (GraphPad) by using Student's t-test. P values less than 0.05 were considered statistically
642 significant. Data from three independent experiments were analyzed.

643 ## Acknowledgments

644 We would like to thank for her technical assistance Valérie Nicolas (Université Paris-Saclay, Châtenay-
645 Malabry, France) from the MIPSIT cellular imaging facility. Also, the present work has benefited from
646 the core facilities of Imagerie-Gif, (http://www.i2bc.paris-saclay.fr), member of IBiSA
647 (http://www.ibisa.net), supported by "France-BioImaging" (ANR- 10-INBS-04-01), and the Labex
648 "Saclay Plant Science" (ANR-11- IDEX-0003-02). We wish to thank Flavie Strappazzon for providing us
649 AMBRA1-ActA plasmid and we are also very grateful to Joëlle Wiels for giving us Ramos cells. Finally,
650 we thank Stephanie Straubel for critical reading of the manuscript.

651 ## Additional information

652 ### Funding

Funder	Grand reference number	Author
CNRS, Univ Paris-Sud, DIM MALINF Région IDF	N/A	Géraldine Vilmen
Agence Nationale de la Recherche	ANR-14-CE14-0022	Audrey Esclatine
The authors declare that the funders had no role in study design, data collection or interpretation, or the decision to submit the work for publication.		

653

654 ## Author contributions

655 DG, GV, DP, GB, conception and design, investigation, formal analysis, writing original draft, writing
656 review and editing; EH, investigation, formal analysis; VM, formal analysis, funding acquisition,
657 supervision; CP, FQ, CBT, formal analysis, provided materials; ML, conception and design, formal
658 analysis, writing original draft, supervision; AE, conception and design, formal analysis, funding
659 acquisition, writing original draft, writing review and editing, supervision.

660 ## Authors ORCIDs

661 Damien Glon : https://orcid.org/0000-0001-8405-8805

662 Daniel Perdiz : https://orcid.org/0000-0002-6804-5980

663 Guillaume Beauclair : https://orcid.org/0000-0001-5323-5987

664 Frédérique Quignon : https://orcid.org/0000-0001-9570-434X

665 Vincent Maréchal : https://orcid.org/0000-0003-2689-6266

666 Christian Poüs : https://orcid.org/0000-0002-2502-7854

667 Marion Lussignol : https://orcid.org/0000-0001-7586-2041

668 Audrey Esclatine : https://orcid.org/0000-0002-4692-5186

669 # Additional files

670 ## Figure supplements

671 - Figure 1 – figure supplement 1. Knockdown of BHRF1 expression in Akata cells prevents mito-
672 aggresome formation after EBV reactivation.
673 - Figure 1 – figure supplement 2. BHRF1 localizes in the proximity of the centrosome.
674 - Figure 1 – figure supplement 3. The actin network is not involved in the formation of BHRF1
675 induced mito-aggresomes.
676 - Figure 3 – figure supplement 1. Impact of the non-acetylatable α-tubulin expression.
677 - Figure 3 – figure supplement 2. MT hyperacetylation required mitochondrial fission.
678 - Figure 4 – figure supplement 1. Interplay between MT hyperacetylation and IFN inhibition in
679 response to different mitophagy inducers.
680 - Figure 5 – figure supplement 1. Loss of ATAT1 has no impact on mitochondrial network.
681 - Figure 5 – figure supplement 2. ATAT1 colocalizes with BHRF1.

682 • Figure 6 – figure supplement 1. Dynein inhibition prevents BHRF1-induced mito-aggresomes.
683 • Figure 7 – figure supplement 1. BHRF1 stimulates autophagy when α-tubulin WT is expressed.
684 • Figure 8 – figure supplement 1. Autophagy inhibition prevents MT hyperacetylation and mito-
685 aggresome formation during EBV reactivation.

686 ## Data availability

687 All data generated or analyzed during this study are included in this published article and its
688 supplementary information files.

689 ## References

690 Altmann M, Hammerschmidt W. 2005. Epstein-Barr Virus Provides a New Paradigm: A Requirement
691 for the Immediate Inhibition of Apoptosis. *PLoS Biol* **3**:e404. doi:10.1371/journal.pbio.0030404
692 Arnoult D, Soares F, Tattoli I, Girardin SE. 2011. Mitochondria in innate immunity. *EMBO Rep* **12**:901–
693 910. doi:10.1038/embor.2011.157
694 Castanier C, Garcin D, Vazquez A, Arnoult D. 2010. Mitochondrial dynamics regulate the RIG-I-like
695 receptor antiviral pathway. *EMBO Rep* **11**:133–138. doi:10.1038/embor.2009.258
696 Chatel-Chaix L, Cortese M, Romero-Brey I, Bender S, Neufeldt CJ, Fischl W, Scaturro P, Schieber N,
697 Schwab Y, Fischer B, Ruggieri A, Bartenschlager R. 2016. Dengue Virus Perturbs Mitochondrial
698 Morphodynamics to Dampen Innate Immune Responses. *Cell Host Microbe* **20**:342–356.
699 doi:10.1016/j.chom.2016.07.008
700 De Vos KJ, Allan VJ, Grierson AJ, Sheetz MP. 2005. Mitochondrial Function and Actin Regulate
701 Dynamin-Related Protein 1-Dependent Mitochondrial Fission. *Curr Biol* **15**:678–683.
702 doi:10.1016/j.cub.2005.02.064
703 Desbien AL, Kappler JW, Marrack P. 2009. The Epstein-Barr virus Bcl-2 homolog, BHRF1, blocks
704 apoptosis by binding to a limited amount of Bim. *Proc Natl Acad Sci U S A* **106**:5663–5668.
705 doi:10.1073/pnas.0901036106
706 Detmer SA, Chan DC. 2007. Functions and dysfunctions of mitochondrial dynamics. *Nat Rev Mol Cell*
707 *Biol* **8**:870–879. doi:10.1038/nrm2275
708 Ding B, Zhang L, Li Z, Zhong Y, Tang Q, Qin Y, Chen M. 2017. The Matrix Protein of Human
709 Parainfluenza Virus Type 3 Induces Mitophagy that Suppresses Interferon Responses. *Cell Host*
710 *& Microbe* **21**:538-547.e4. doi:10.1016/j.chom.2017.03.004
711 Dompierre JP, Godin JD, Charrin BC, Cordelieres FP, King SJ, Humbert S, Saudou F. 2007. Histone
712 Deacetylase 6 Inhibition Compensates for the Transport Deficit in Huntington's Disease by
713 Increasing Tubulin Acetylation. *J Neurosci* **27**:3571–3583. doi:10.1523/JNEUROSCI.0037-07.2007
714 Eshun-Wilson L, Zhang R, Portran D, Nachury MV, Toso DB, Löhr T, Vendruscolo M, Bonomi M, Fraser
715 JS, Nogales E. 2019. Effects of α-tubulin acetylation on microtubule structure and stability. *Proc*
716 *Natl Acad Sci U S A* **116**:10366–10371. doi:10.1073/pnas.1900441116
717 Esteves AR, Palma AM, Gomes R, Santos D, Silva DF, Cardoso SM. 2019. Acetylation as a major
718 determinant to microtubule-dependent autophagy: Relevance to Alzheimer's and Parkinson
719 disease pathology. *Biochim Biophys Acta*, Post-Translational Modifications In Brain Health And
720 Disease **1865**:2008–2023. doi:10.1016/j.bbadis.2018.11.014
721 Etienne-Manneville S, Hall A. 2001. Integrin-mediated activation of Cdc42 controls cell polarity in
722 migrating astrocytes through PKCzeta. *Cell* **106**:489–498. doi:10.1016/s0092-8674(01)00471-8
723 Fitzsimmons L, Kelly G. 2017. EBV and Apoptosis: The Viral Master Regulator of Cell
724 Fate? *Viruses* **9**:339–373. doi:10.3390/v9110339

725 Fransson Å, Ruusala A, Aspenström P. 2006. The atypical Rho GTPases Miro-1 and Miro-2 have
726 essential roles in mitochondrial trafficking. *Biochem Biophys Res Commun* **344**:500–510.
727 doi:10.1016/j.bbrc.2006.03.163
728 Frederick RL, Shaw JM. 2007. Moving Mitochondria: Establishing Distribution of an Essential
729 Organelle. *Traffic* **8**:1668–1675. doi:10.1111/j.1600-0854.2007.00644.x
730 Friedman JR, Webster BM, Mastronarde DN, Verhey KJ, Voeltz GK. 2010. ER sliding dynamics and ER–
731 mitochondrial contacts occur on acetylated microtubules. *J Cell Biol* **190**:363–375.
732 doi:10.1083/jcb.200911024
733 Geeraert C, Ratier A, Pfisterer SG, Perdiz D, Cantaloube I, Rouault A, Pattingre S, Proikas-Cezanne T,
734 Codogno P, Poüs C. 2010. Starvation-induced Hyperacetylation of Tubulin Is Required for the
735 Stimulation of Autophagy by Nutrient Deprivation. *J Biol Chem* **285**:24184–24194.
736 doi:10.1074/jbc.M109.091553
737 Green DR, Levine B. 2014. To Be or Not to Be? How Selective Autophagy and Cell Death Govern Cell
738 Fate. *Cell* **157**:65–75. doi:10.1016/j.cell.2014.02.049
739 Hancock WO. 2014. Bidirectional cargo transport: moving beyond tug of war. *Nat Rev Mol Cell*
740 *Biol* **15**:615–628. doi:10.1038/nrm3853
741 Hubbert C, Guardiola A, Shao R, Kawaguchi Y, Ito A, Nixon A, Yoshida M, Wang X-F, Yao T-P. 2002.
742 HDAC6 is a microtubule-associated deacetylase. *Nature* **417**:455–458. doi:10.1038/417455a
743 Janke C, Magiera MM. 2020. The tubulin code and its role in controlling microtubule properties and
744 functions. *Nat Rev Mol Cell Biol* **21**:307–326. doi:10.1038/s41580-020-0214-3
745 Janke C, Montagnac G. 2017. Causes and Consequences of Microtubule Acetylation. *Curr*
746 *Biol* **27**:1287–1292. doi:10.1016/j.cub.2017.10.044
747 Kaufmann T, Kukolj E, Brachner A, Beltzung E, Bruno M, Kostrhon S, Opravil S, Hudecz O, Mechtler K,
748 Warren G, Slade D. 2016. SIRT2 regulates nuclear envelope reassembly through ANKLE2
749 deacetylation. *J Cell Sci* **129**:4607–4621. doi:10.1242/jcs.192633
750 Kearns NA, Genga RMJ, Enuameh MS, Garber M, Wolfe SA, Maehr R. 2014. Cas9 effector-mediated
751 regulation of transcription and differentiation in human pluripotent stem
752 cells. *Development* **141**:219–223. doi:10.1242/dev.103341
753 Khanim F, Mackett M, Young LS, Dawson J, Meseda CA, Dawson C. 1997. BHRF1, a viral homologue of
754 the Bcl-2 oncogene, is conserved at both the sequence and functional level in different Epstein-
755 Barr virus isolates. *J Gen Virol* **78**:2987–2999. doi:10.1099/0022-1317-78-11-2987
756 Köchl R, Hu XW, Chan EYW, Tooze SA. 2006. Microtubules Facilitate Autophagosome Formation and
757 Fusion of Autophagosomes with Endosomes: Role of Microtubules in AV
758 Formation. *Traffic* **7**:129–145. doi:10.1111/j.1600-0854.2005.00368.x
759 Koopman WJH, Visch H-J, Smeitink JAM, Willems PHGM. 2006. Simultaneous quantitative
760 measurement and automated analysis of mitochondrial morphology, mass, potential, and
761 motility in living human skin fibroblasts. *Cytometry Part A* **69A**:1–12. doi:10.1002/cyto.a.20198
762 Kruppa AJ, Buss F. 2021. Motor proteins at the mitochondria-cytoskeleton interface. *J Cell Sci* **134**:1–
763 13. doi:10.1242/jcs.226084
764 Kvansakul M, Wei AH, Fletcher JI, Willis SN, Chen L, Roberts AW, Huang DCS, Colman PM. 2010.
765 Structural Basis for Apoptosis Inhibition by Epstein-Barr Virus BHRF1. *PLoS Pathog* **6**:e1001236.
766 doi:10.1371/journal.ppat.1001236
767 Lazarou M, Sliter DA, Kane LA, Sarraf SA, Wang C, Burman JL, Sideris DP, Fogel AI, Youle RJ. 2015. The
768 ubiquitin kinase PINK1 recruits autophagy receptors to induce mitophagy. *Nature* **524**:309–314.
769 doi:10.1038/nature14893
770 Lee AJ, Ashkar AA. 2018. The Dual Nature of Type I and Type II Interferons. *Front Immunol* **9**:2061–
771 2070. doi:10.3389/fimmu.2018.02061
772 López-Doménech G, Covill-Cooke C, Ivankovic D, Halff EF, Sheehan DF, Norkett R, Birsa N, Kittler JT.
773 2018. Miro proteins coordinate microtubule- and actin-dependent mitochondrial transport and
774 distribution. *EMBO J* **37**:321–336. doi:10.15252/embj.201696380

775 Luo S, Garcia-Arencibia M, Zhao R, Puri C, Toh PPC, Sadiq O, Rubinsztein DC. 2012. Bim inhibits
776 autophagy by recruiting Beclin 1 to microtubules. *Mol Cell* **47**:359–370.
777 doi:10.1016/j.molcel.2012.05.040
778 Mackeh R, Lorin S, Ratier A, Mejdoubi-Charef N, Baillet A, Bruneel A, Hamaï A, Codogno P, Poüs C,
779 Perdiz D. 2014. Reactive Oxygen Species, AMP-activated Protein Kinase, and the Transcription
780 Cofactor p300 Regulate α-Tubulin Acetyltransferase-1 (αTAT-1/MEC-17)-dependent
781 Microtubule Hyperacetylation during Cell Stress. *J Biol Chem* **289**:11816–11828.
782 doi:10.1074/jbc.M113.507400
783 Mackeh R, Perdiz D, Lorin S, Codogno P, Pous C. 2013. Autophagy and microtubules - new story, old
784 players. *J Cell Sci* **126**:1071–80. doi:10.1242/jcs.115626
785 Misawa T, Takahama M, Kozaki T, Lee H, Zou J, Saitoh T, Akira S. 2013. Microtubule-driven spatial
786 arrangement of mitochondria promotes activation of the NLRP3 inflammasome. *Nat*
787 *Immunol* **14**:454–460. doi:10.1038/ni.2550
788 Narendra D, Kane LA, Hauser DN, Fearnley IM, Youle RJ. 2010. p62/SQSTM1 is required for Parkin-
789 induced mitochondrial clustering but not mitophagy; VDAC1 is dispensable for
790 both. *Autophagy* **6**:1090–1106. doi:10.4161/auto.6.8.13426
791 Narendra DP, Tanaka A, Suen D-F, Youle RJ. 2008. Parkin is recruited selectively to impaired
792 mitochondria and promotes their autophagy. *J Cell Biol* **183**:795–803.
793 doi:10.1083/jcb.200809125
794 Nowosad A, Creff J, Jeannot P, Culerrier R, Codogno P, Manenti S, Nguyen L, Besson A. 2021. p27
795 controls autophagic vesicle trafficking in glucose-deprived cells via the regulation of ATAT1-
796 mediated microtubule acetylation. *Cell Death Dis* **12**:1–18. doi:10.1038/s41419-021-03759-9
797 Perdiz D, Lorin S, Leroy-Gori I, Poüs C. 2017. Stress-induced hyperacetylation of microtubule
798 enhances mitochondrial fission and modulates the phosphorylation of Drp1 at 616 Ser. *Cell*
799 *Signalling* **39**:32–43. doi:10.1016/j.cellsig.2017.07.020
800 Perdiz D, Mackeh R, Poüs C, Baillet A. 2011. The ins and outs of tubulin acetylation: More than just a
801 post-translational modification? *Cell Signalling* **23**:763–771. doi:10.1016/j.cellsig.2010.10.014
802 Portran D, Schaedel L, Xu Z, Théry M, Nachury MV. 2017. Tubulin acetylation protects long-lived
803 microtubules against mechanical ageing. *Nat Cell Biol* **19**:391–398. doi:10.1038/ncb3481
804 Puthalakath H, Huang DCS, O'Reilly LA, King SM, Strasser A. 1999. The Proapoptotic Activity of the
805 Bcl-2 Family Member Bim Is Regulated by Interaction with the Dynein Motor Complex. *Mol*
806 *Cell* **3**:287–296. doi:10.1016/S1097-2765(00)80456-6
807 Reed NA, Cai D, Blasius TL, Jih GT, Meyhofer E, Gaertig J, Verhey KJ. 2006. Microtubule Acetylation
808 Promotes Kinesin-1 Binding and Transport. *Curr Biol* **16**:2166–2172.
809 doi:10.1016/j.cub.2006.09.014
810 Roberts AJ, Kon T, Knight PJ, Sutoh K, Burgess SA. 2013. Functions and mechanics of dynein motor
811 proteins. *Nat Rev Mol Cell Biol* **14**:713–726. doi:10.1038/nrm3667
812 Shaner NC, Campbell RE, Steinbach PA, Giepmans BNG, Palmer AE, Tsien RY. 2004. Improved
813 monomeric red, orange and yellow fluorescent proteins derived from Discosoma sp. red
814 fluorescent protein. *Nat Biotechnol* **22**:1567–1572. doi:10.1038/nbt1037
815 Shida T, Cueva JG, Xu Z, Goodman MB, Nachury MV. 2010. The major α-tubulin K40 acetyltransferase
816 αTAT1 promotes rapid ciliogenesis and efficient mechanosensation. *Proc Natl Acad Sci U S*
817 *A* **107**:21517–21522. doi:10.1073/pnas.1013728107
818 Singh PK, Weber A, Häcker G. 2018. The established and the predicted roles of dynein light chain in
819 the regulation of mitochondrial apoptosis. *Cell Cycle* **17**:1037–1047.
820 doi:10.1080/15384101.2018.1464851
821 Strappazzon F, Nazio F, Corrado M, Cianfanelli V, Romagnoli A, Fimia GM, Campello S, Nardacci R,
822 Piacentini M, Campanella M, Cecconi F. 2015. AMBRA1 is able to induce mitophagy via LC3
823 binding, regardless of PARKIN and p62/SQSTM1. *Cell Death Differ* **22**:419–32.
824 doi:10.1038/cdd.2014.139
825 Tang B. 2018. Miro—Working beyond Mitochondria and Microtubules. *Cells* **7**:18–24.
826 doi:10.3390/cells7030018

827 Vilmen G, Glon D, Siracusano G, Lussignol M, Shao Z, Hernandez E, Perdiz D, Quignon F, Mouna L,
828 Poüs C, Gruffat H, Maréchal V, Esclatine A. 2020. BHRF1, a BCL2 viral homolog, disturbs
829 mitochondrial dynamics and stimulates mitophagy to dampen type I IFN
830 induction. *Autophagy* **17**:1296–1315. doi:10.1080/15548627.2020.1758416
831 Walker RA, O'Brien E. T, Pryer NK, Soboeiro MF, Voter WA, Erickson HP, Salmon ED. 1988. Dynamic
832 instability of individual microtubules analyzed by video light microscopy: rate constants and
833 transition frequencies. *J Cell Biol* **107**:1437–1448. doi:10.1083/jcb.107.4.1437
834 Wang K, Ma H, Liu H, Ye W, Li Z, Cheng L, Zhang L, Lei Y, Shen L, Zhang F. 2019. The Glycoprotein and
835 Nucleocapsid Protein of Hantaviruses Manipulate Autophagy Flux to Restrain Host Innate
836 Immune Responses. *Cell Reports* **27**:2075-2091.e5. doi:10.1016/j.celrep.2019.04.061
837 Wang R, Zhu Y, Ren C, Yang S, Tian S, Chen H, Jin M, Zhou H. 2020. Influenza A virus protein PB1-F2
838 impairs innate immunity by inducing mitophagy. *Autophagy* 1–16.
839 doi:10.1080/15548627.2020.1725375
840 West AP, Shadel GS, Ghosh S. 2011. Mitochondria in innate immune responses. *Nat Rev*
841 *Immunol* **11**:389–402. doi:10.1038/nri2975
842 Xie R, Nguyen S, McKeehan WL, Liu L. 2010. Acetylated microtubules are required for fusion of
843 autophagosomes with lysosomes. *BMC Cell Biol* **11**:89–100. doi:10.1186/1471-2121-11-89
844 Yoneyama M, Kikuchi M, Natsukawa T, Shinobu N, Imaizumi T, Miyagishi M, Taira K, Akira S, Fujita T.
845 2004. The RNA helicase RIG-I has an essential function in double-stranded RNA-induced innate
846 antiviral responses. *Nat Immunol* **5**:730–737. doi:10.1038/ni1087
847 Yoneyama M, Suhara W, Fukuhara Y, Sato M, Ozato K, Fujita T. 1996. Autocrine Amplification of Type
848 I Interferon Gene Expression Mediated by Interferon Stimulated Gene Factor 3 (ISGF3). *J*
849 *Biochem* **120**:160–169. doi:10.1093/oxfordjournals.jbchem.a021379
850 Yoshizumi T, Ichinohe T, Sasaki O, Otera H, Kawabata S, Mihara K, Koshiba T. 2014. Influenza A virus
851 protein PB1-F2 translocates into mitochondria via Tom40 channels and impairs innate
852 immunity. *Nat Commun* **5**:4713. doi:10.1038/ncomms5713
853 Zheng K, Jiang Y, He Z, Kitazato K, Wang Y. 2017. Cellular defence or viral assist: the dilemma of
854 HDAC6. *J Gen Virol* **98**:322–337. doi:10.1099/jgv.0.000679

855 **Words count**: 10484

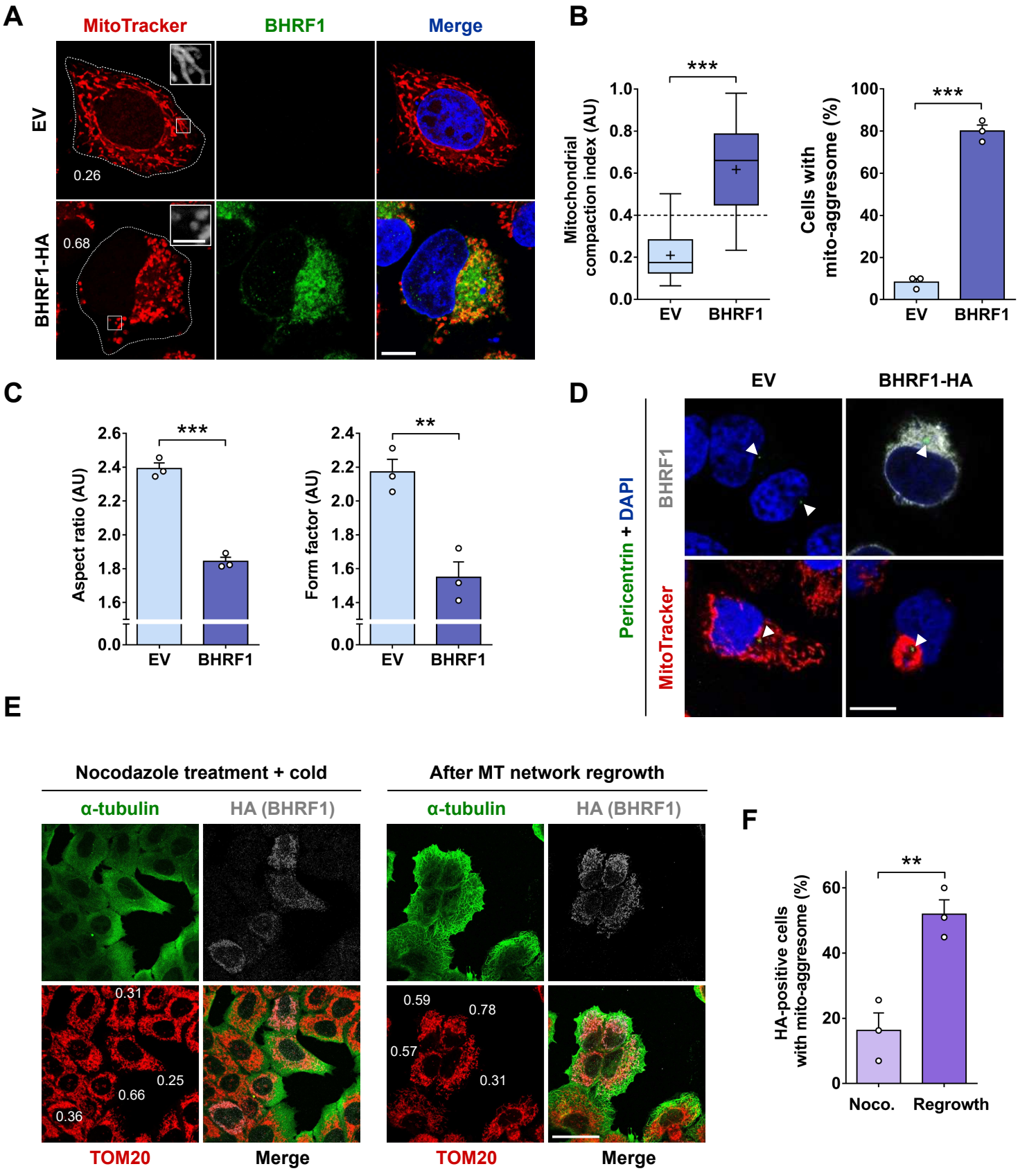

Figure 1. BHRF1 induces the formation of mito-aggresomes in a MT-dependent manner. (**A-C**) HeLa cells were transfected for 24 h with BHRF1-HA plasmid or with EV as a control. Mitochondria were labeled with MitoTracker and cells immunostained for BHRF1. Nuclei were stained with DAPI. (**A**) Confocal images with insets (3X) on mitochondrial phenotype. Values of mitochondrial CI are indicated on representative cells. Scale bars: 10 µm and 2 µm for insets. (**B**) *Left*, assessment of mitochondrial aggregation by calculation of CI. *Right*, percentage of cells presenting a mito-aggresome (n = 20 cells per condition). (**C**) Quantification of mitochondrial fission parameters, aspect ratio (AR; *left panel*) and form factor (FF, *right panel*). (**D**) Confocal images of HeLa cells transfected with BHRF1-HA plasmid (or EV) and immunostained for pericentrin and BHRF1 (*upper panel*) or mitochondria (*lower panel*). Nuclei were stained with DAPI. Scale bar: 20 µm. Arrowheads show the centrosomal localization of pericentrin. (**E-F**) MT network depolymerization assay. (**E**) Representative images where BHRF1 expression was visualized by HA immunostaining (gray), the MT network by α-tubulin immunostaining (green), and mitochondria are immunostained with an anti-TOM20 antibody (red). Values of mitochondrial CI are indicated on representative cells. Scale bars: 10 µm. (**F**) Percentage of BHRF1-HA-positive cells presenting a mito-aggresome (n = 30 cells per condition) in cells treated with nocodazole and after MT regrowth.
Data represent the mean ± SEM of three independent experiments. ** P < 0.01; *** P < 0.001 (Student's t-test).

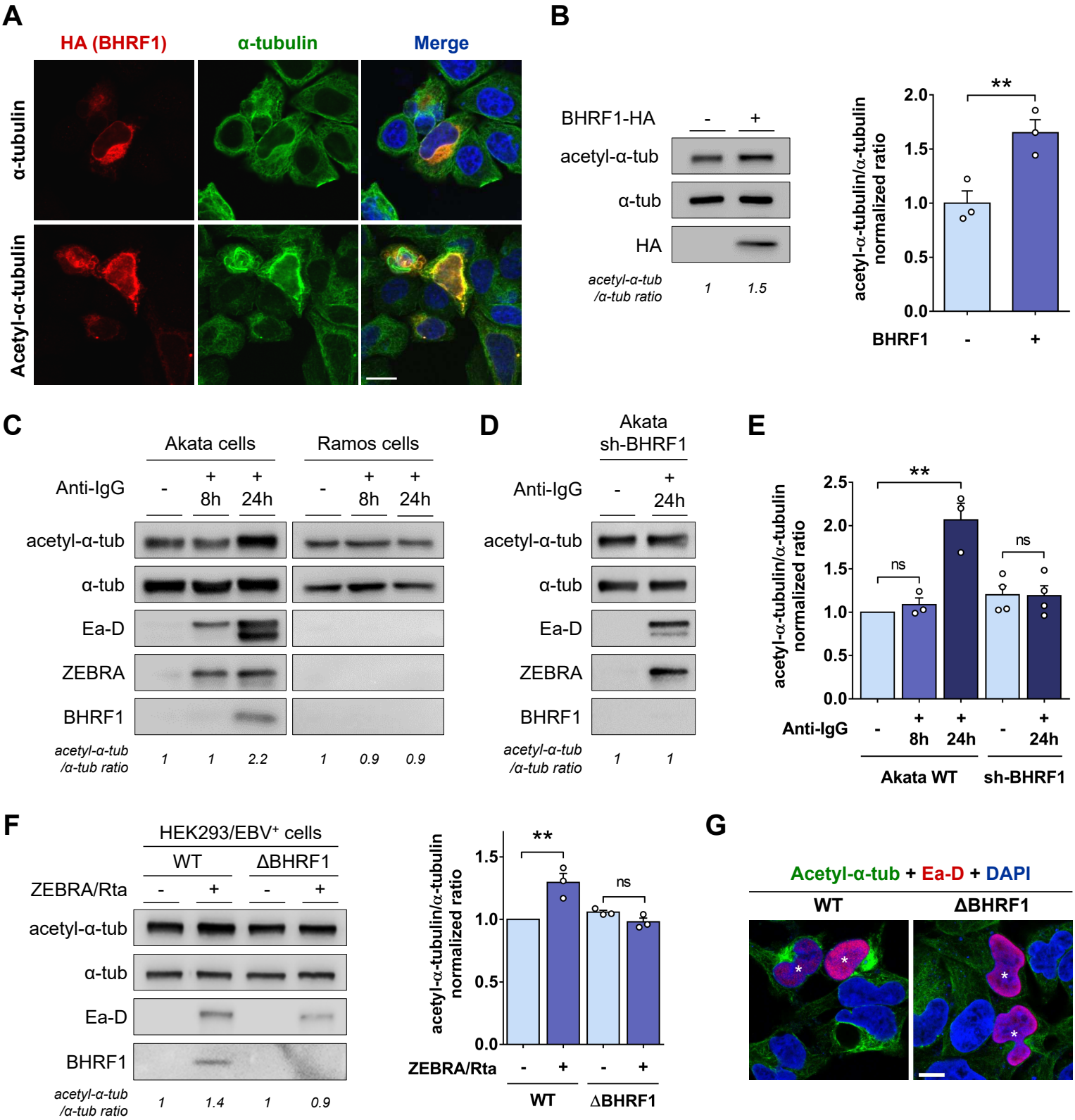

Figure 2. BHRF1 stimulates MT hyperacetylation. (**A**) Representative images of HeLa cells expressing BHRF1-HA and immunostained for HA and α-tubulin (*upper panel)* or acetyl-α-tubulin (*lower panel*). Nuclei were stained with DAPI. Scale bar: 20 µm. (**B**) *Left*, immunoblot analysis of acetyl and total α-tubulin in BHRF1-HA-transfected HeLa cells. *Right*, normalized ratios of acetyl-α-tubulin to total α-tubulin. (**C**) Immunoblot analysis of acetyl-α-tubulin, α-tubulin, Ea-D, ZEBRA and BHRF1 in the Akata and Ramos cells treated or not with anti-human IgG for 8 h or 24 h to induce EBV reactivation. (**D**) Immunoblot analysis of acetyl-α-tubulin, α-tubulin, Ea-D, ZEBRA and BHRF1 in Akata cells deficient for BHRF1 expression (sh-BHRF1). (**E**) Normalized ratios of acetyl-α-tubulin to α-tubulin in Akata cells. (**F-G**) EBV WT or EBV ΔBHRF1 were reactivated in HEK293 cells by transfection with ZEBRA and Rta plasmids for 24 h. (**F**) *Left*, immunoblot analysis of acetyl-α-tubulin, α-tubulin, Ea-D and BHRF1. *Right*, normalized ratios of acetyl-α-tubulin to α-tubulin. (**G**) Confocal images of HEK293/EBV+ cells immunostained for acetyl-α-tubulin and Ea-D. Nuclei were stained with DAPI. Scale bar: 20 µm. Stars indicate EBV-reactivated cells.
Data represent the mean ± SEM of three independent experiments. ns = non-significant; ** $P < 0.01$ (Student's t-test).

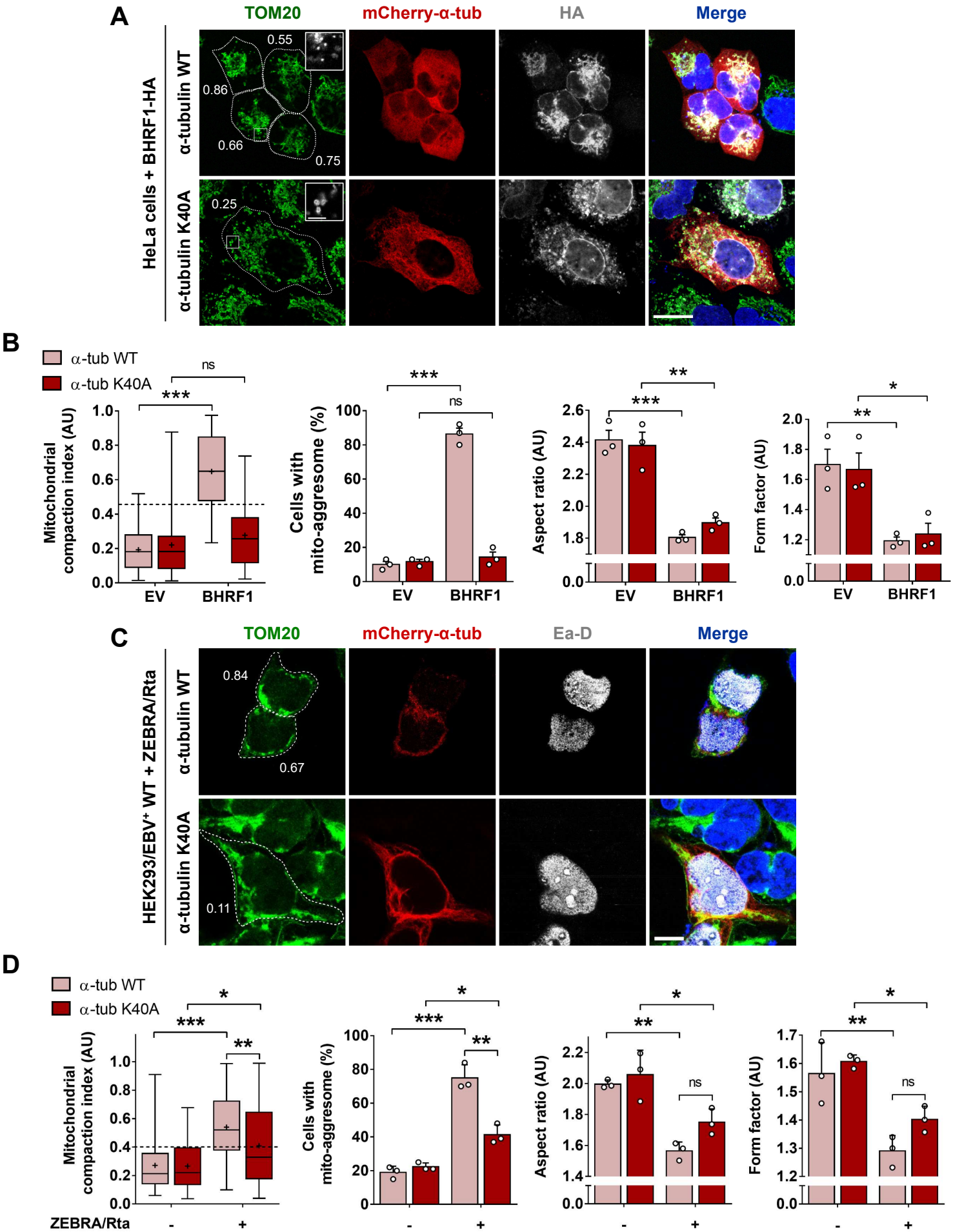

Figure 3. MT hyperacetylation is required for BHRF1-induced mito-aggresomes formation. (**A-B**) HeLa cells were co-transfected with plasmids encoding BHRF1-HA and either mCherry-α-tubulin WT or a non-acetylatable form (K40A). (**A**) Confocal images with insets (3X) of cells immunostained for HA and TOM20. Nuclei were stained with DAPI. Scale bars: 10 µm and 4 µm for insets. Values of mitochondrial CI are indicated on representative cells. Images of control cells are presented in Figure 3 – figure supplement 1B. (**B**) Quantification of CI, percentage of cells with a mito-aggresome and mitochondrial fission parameters (n = 20 cells per condition). (**C-D**) HEK293/EBV+ WT cells were co-transfected with plasmids encoding ZEBRA, Rta and either mCherry-α-tubulin WT or K40A. (**C**) Confocal images of cells immunostained for Ea-D and TOM20. Nuclei were stained with DAPI. Scale bar: 10 µm. Values of mitochondrial CI are indicated on representative cells. (**D**) Quantification of CI, percentage of cells with a mito-aggresome and mitochondrial fission parameters (n = 20 cells per condition).
Data represent the mean ± SEM of three independent experiments. ns = non-significant; * P < 0.05; ** P < 0.01; *** P < 0.001 (Student's t-test).

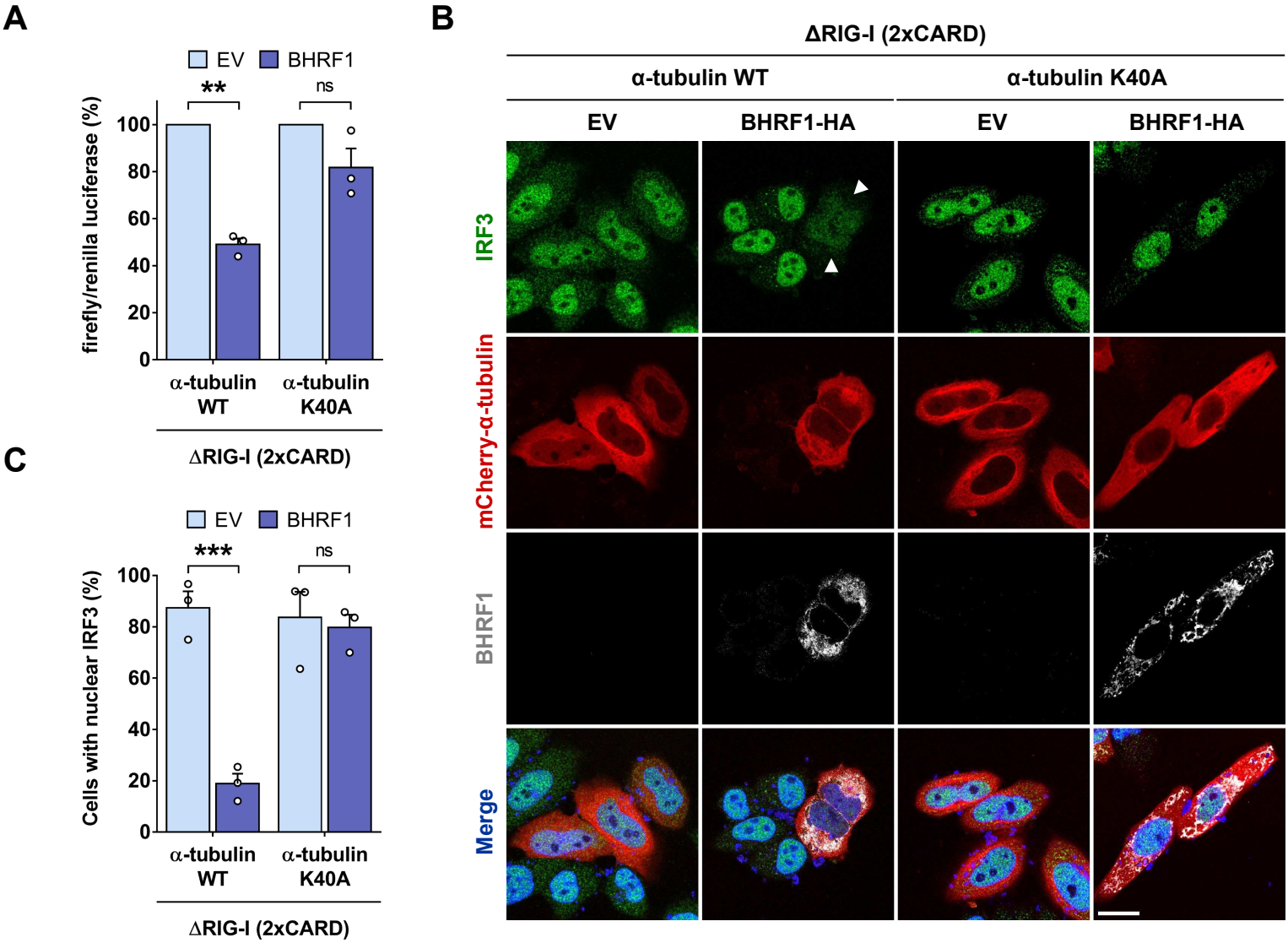

Figure 4. MT hyperacetylation is required for BHRF1 to block IFN. (**A**) Luciferase reporter assay on HEK293T cells co-expressing BHRF1 (or EV) and α-tubulin K40A (or WT). Activation of the IFN-β promoter was analyzed 24 h post-transfection. Firefly/renilla luciferase ratios were calculated and normalized to control conditions. (**B-C**) HeLa cells were co-transfected for 24 h with plasmids encoding BHRF1-HA (or EV), mCherry-α-tubulin K40A (or WT), and ΔRIG-I (2xCARD). (**B**) Confocal images. BHRF1-HA-transfected cells were visualized with an anti-HA antibody and cells were immunostained with an-anti IRF3 antibody. Nuclei were stained with DAPI. Scale bar: 20 µm. Arrows indicate BHRF1-expressing cells without IRF3 nuclear localization. (**C**) Percentage of cells expressing mCherry-α-tubulin and presenting IRF3 nuclear localization (n = 50 cells per condition). Data represent the mean ± SEM of three independent experiments. ns = non-significant; ** $P < 0.01$; *** $P < 0.001$ (Student's t-test).

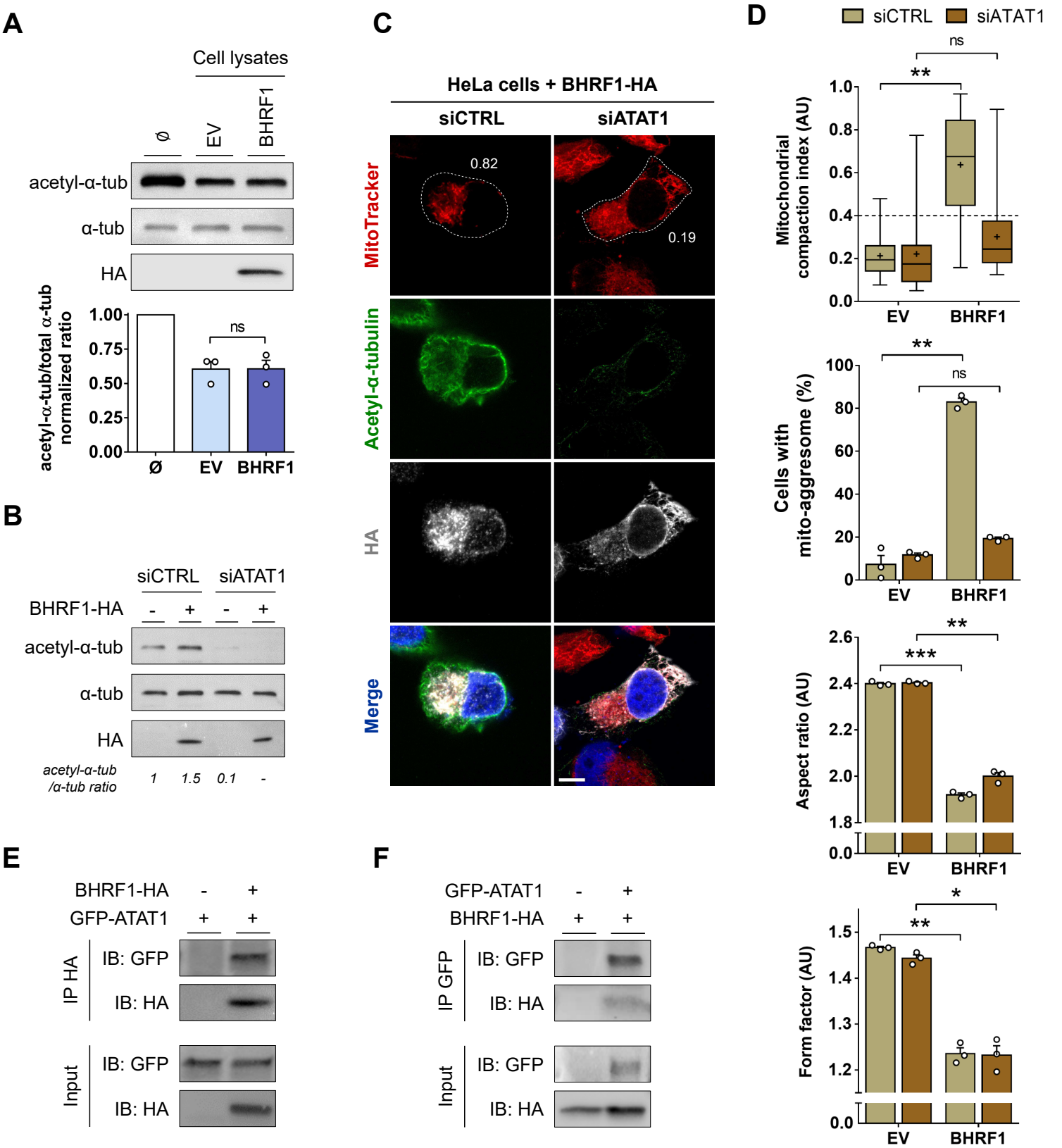

Figure 5. MT hyperacetylation and mito-aggresome formation require ATAT1, which interacts with BHRF1. (**A**) Tubulin deacetylation assay. HeLa cells were transfected with BHRF1-HA plasmid (or EV) and lysed 48 h post-transfection. Cell lysates were incubated in vitro with porcine brain tubulin and NAD+. BHRF1-HA, acetyl-α-tubulin and α-tubulin were detected by immunoblot, and the histograms represent the normalized ratios of acetyl-α-tubulin to α-tubulin. (**B-D**) After knockdown of ATAT1 by siRNA transfection, HeLa cells were transfected with BHRF1-HA for 24 h. (**B**) Loss of ATAT1 activity was visualized by immunoblot analysis of acetyl-α-tubulin and α-tubulin. (**C**) Confocal images. Mitochondria were labeled with MitoTracker, and cells were immunostained for acetyl-α-tubulin and HA. Nuclei were stained with DAPI. Values of mitochondrial CI are indicated on representative cells. Scale bar: 20 µm. Images of EV-transfected cells are presented in *Figure 5 – figure supplement 1*. (**D**) Quantification of CI, percentage of cells with a mito-aggresome and mitochondrial fission parameters (n = 20 cells per condition). (**E-F**) HeLa cells were co-transfected with GFP-ATAT1 and BHRF1-HA plasmids for 24 h. (**E**) After immunoprecipitation of BHRF1 with an anti-HA antibody, proteins were detected by immunoblotting with anti-GFP and anti-HA antibodies. (**F**) After immunoprecipitation of GFP-ATAT1 with an anti-GFP antibody, proteins were detected by immunoblotting with anti-GFP and anti-HA antibodies.
Data represent the mean ± SEM of three independent experiments. ns = non-significant; * P < 0.05; ** P < 0.01; *** P < 0.001 (Student's t-test).

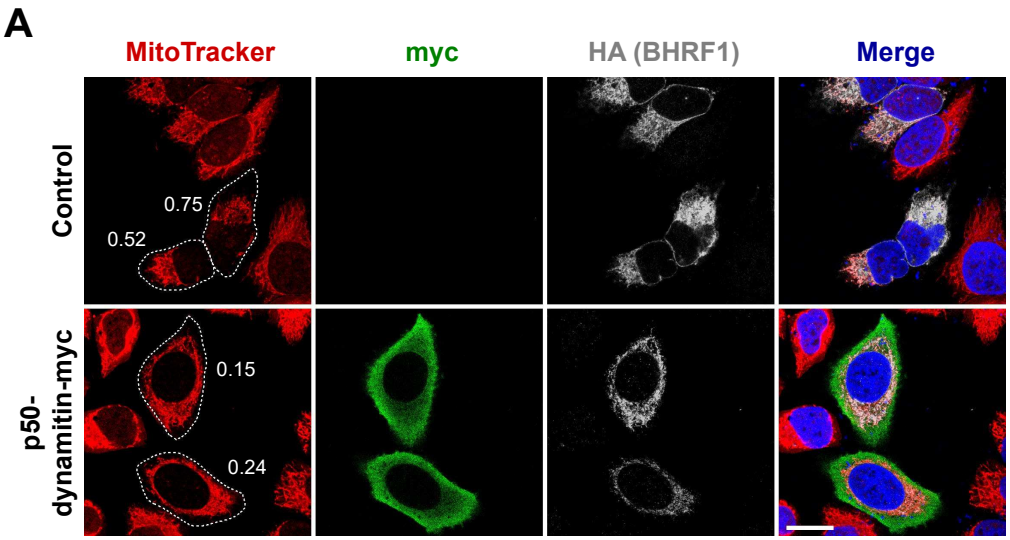

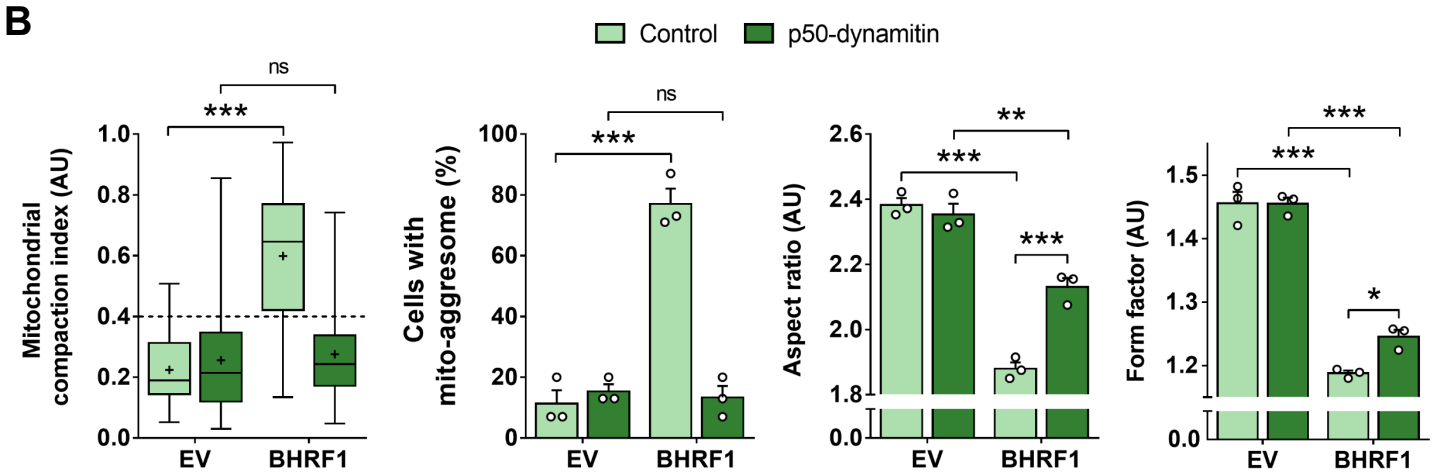

Figure 6. Dynein-based transport is required for BHRF1 to aggregate mitochondria next to the nucleus. (**A-B**) HeLa cells were co-transfected with plasmids encoding BHRF1-HA and p50-dynamitin-myc (or control) for 24 h. (**A**) Confocal images. Mitochondria were labeled with MitoTracker, and cells were immunostained for c-myc and HA. Nuclei were stained with DAPI. Values of mitochondrial CI are indicated on representative cells. Scale bar: 20 µm. Images of cells co-expressing EV and p50-dynamitin-myc are presented in Figure 6 – figure supplement 1A. (**B**) Quantification of CI, percentage of cells with a mito-aggresome and mitochondrial fission parameters (n = 20 cells per condition).
Data represent the mean ± SEM of three independent experiments. ns = non-significant; * P < 0.05, ** P < 0.01; *** P < 0.001 (Student's t-test).

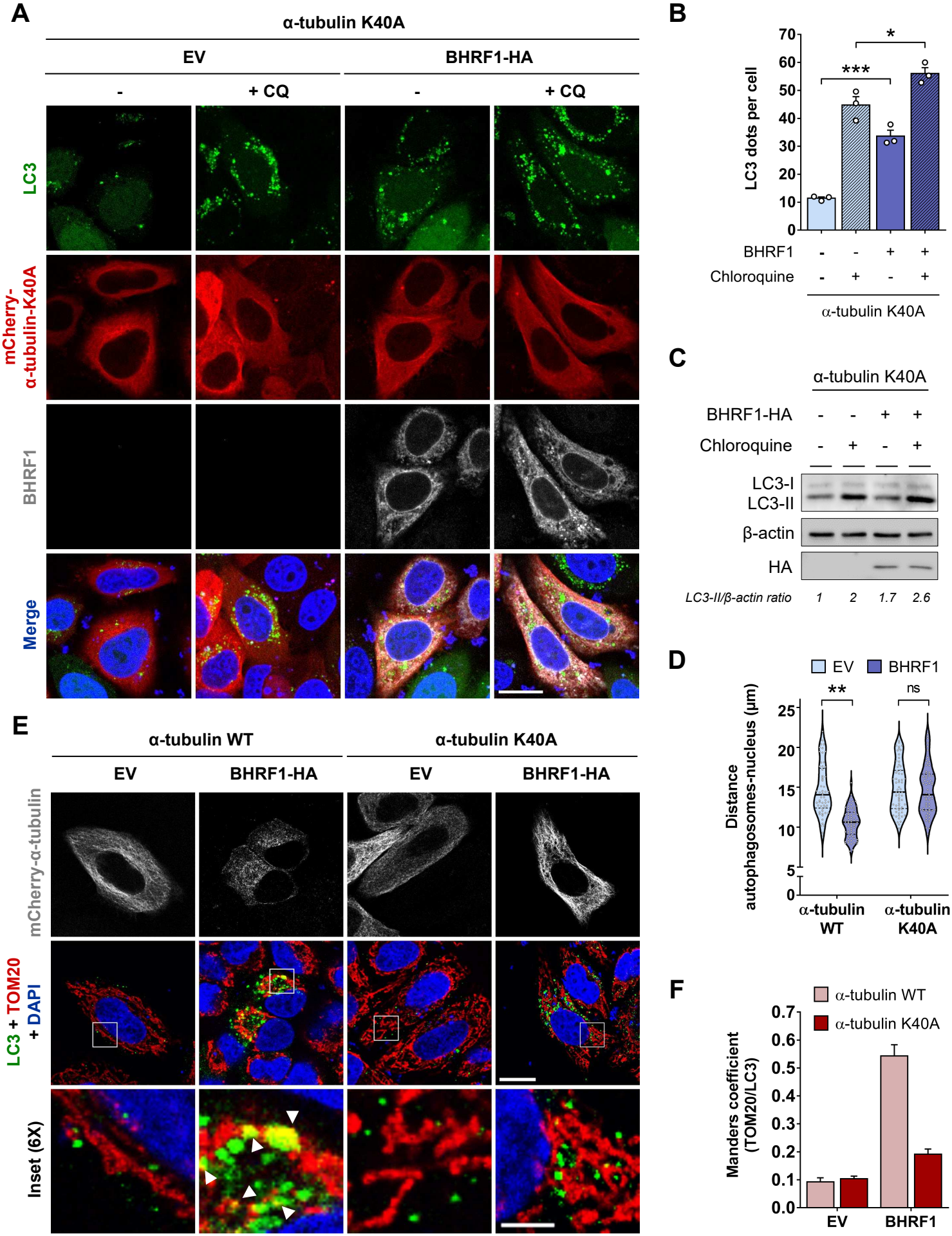

Figure 7. MT hyperacetylation is dispensable for BHRF1-pro-autophagic activity, but essential for mitophagy. HeLa cells were co-transfected for 24 h with plasmids encoding BHRF1-HA (or EV) and mCherry-α-tubulin K40A (or WT) and treated with chloroquine when indicated. (**A**) Confocal images. Cells were immunostained for BHRF1 and LC3 and nuclei stained with DAPI. Scale bar: 10 µm. Images of cells transfected with mCherry-α-tubulin WT are presented in Figure 7 – figure supplement 1A. (**B**) Quantification of LC3 dots (n = 30 cells per condition). (**C**) Immunoblot analysis of LC3 and BHRF1-HA expression. β-actin was used as a loading control. (**D**) Measurement of the distance between autophagosomes and nucleus (n = 60 cells from three independent experiments). (**E**) Confocal images of cells immunostained for TOM20 and LC3. Nuclei were stained with DAPI. Insets (6X) show colocalization events (see arrows). Scale bars: 10 µm and 5 µm for insets. (**F**) Colocalization level (Manders coefficient) between mitochondria (TOM20) and autophagosomes (LC3) (n = 30 cells per condition).
Data represent the mean ± SEM of three independent experiments. ns = non-significant; * P < 0.05, ** P < 0.01; *** P < 0.001 (Student's t-test).

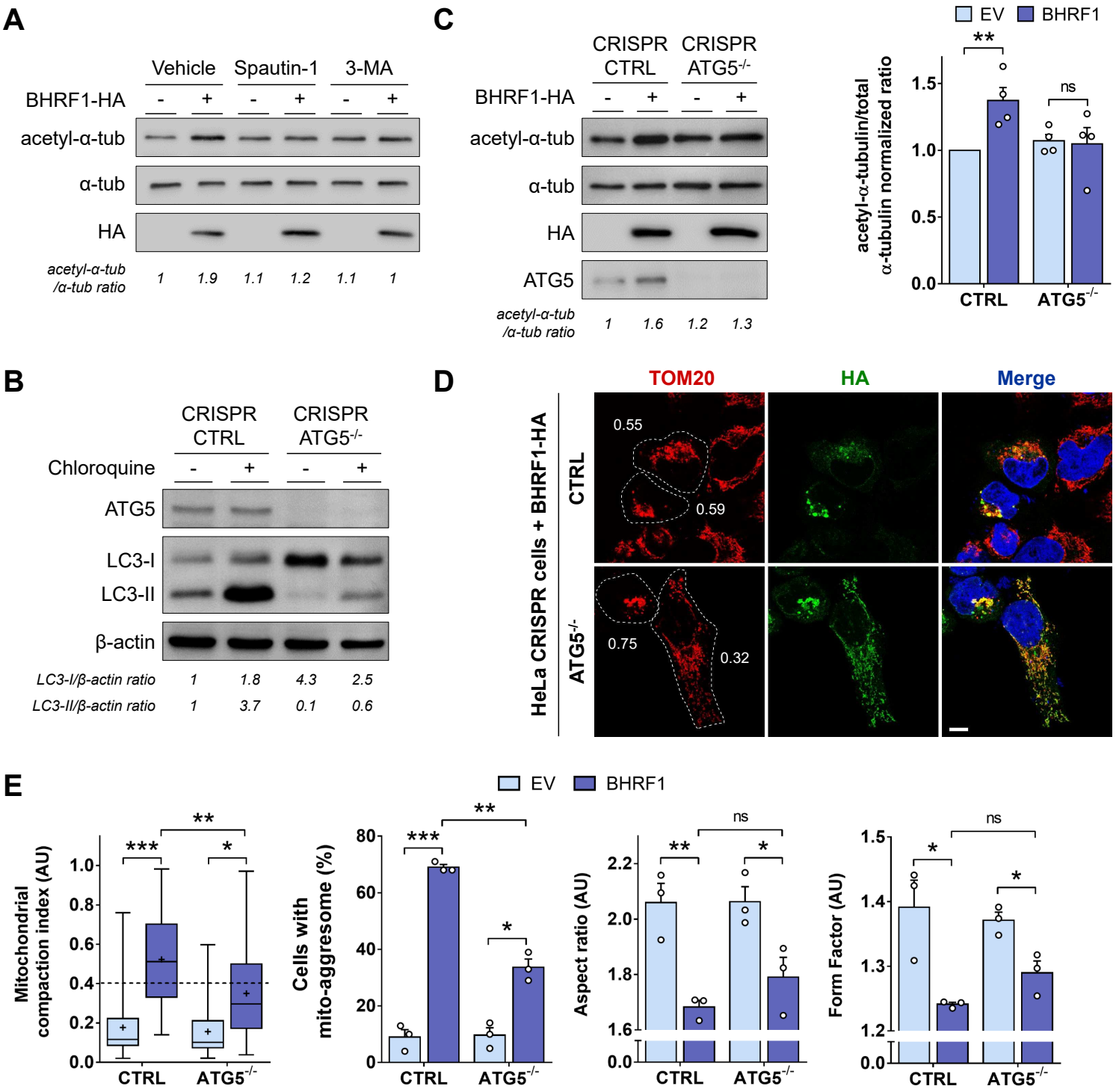

Figure 8. Autophagy inhibition prevents BHRF1-induced hyperacetylation and mito-aggresome formation. (**A**) Immunoblot analysis of acetyl-α-tubulin and α-tubulin of HeLa cells transfected with BHRF1-HA and treated or not with autophagic inhibitors (spautin-1 or 3-MA). (**B**) Control of the autophagy level and ATG5 extinction in HeLa cells treated or not with chloroquine. Immunoblot analysis of ATG5 and LC3. β-actin was used as a loading control. (**C-E**) HeLa cells deficient ATG5 (CRISPR ATG5-/-) and control cells (CRISPR CTRL) were transfected with BHRF1-HA for 24 h. (**C**) Left, immunoblot analysis of acetyl-α-tubulin, α-tubulin, HA and ATG5. Right, normalized ratios of acetyl-α-tubulin to α-tubulin. (**D**) Confocal images of cells immunostained for TOM20 and HA. Nuclei were stained with DAPI. Values of mitochondrial CI are indicated on representative cells. Scale bar: 10 µm. (**E**) Quantification of CI, percentage of cells with a mito-aggresome and mitochondrial fission parameters (n = 20 cells per condition).

Data represent the mean ± SEM of three independent experiments. ns = non-significant; * $P < 0.05$; ** $P < 0.01$; *** $P < 0.001$ (Student's t-test).

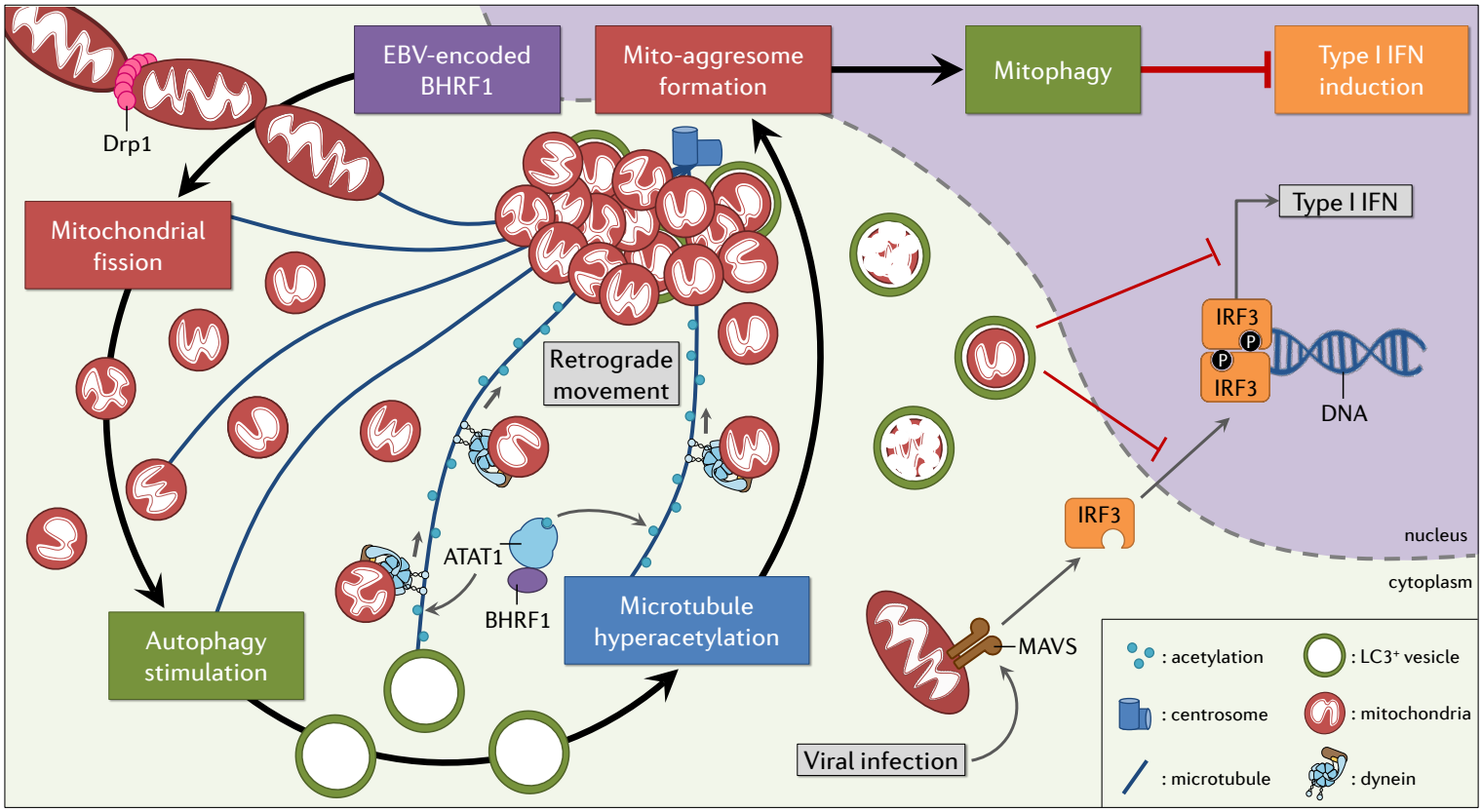

Figure 9. Working model. EBV encodes a Bcl-2 homolog that dampens type I IFN induction thanks to MT hyperacetylation. BHRF1 induces Drp1-mediated mitochondrial fission and subsequently autophagy. These cellular modifications lead to the mito-aggresome formation, and we demonstrated that the MT network and in particular its acetylation level are essential for this mitochondrial phenotype. Moreover, BHRF1 interacts with ATAT1 and induces MT hyperacetylation through ATAT1 activation. This hyperacetylation allows the retrograde transport of mitochondria in a dynein-dependent manner. Finally, sequestration and degradation of mitochondria block the innate immunity.